Since January 2020 Elsevier has created a COVID-19 resource centre with free information in English and Mandarin on the novel coronavirus COVID-19. The COVID-19 resource centre is hosted on Elsevier Connect, the company's public news and information website.

Biomaterials 283 (2022) 121393

Contents lists available at ScienceDirect

Biomaterials

journal homepage: www.elsevier.com/locate/biomaterials

DAMPs/PAMPs induce monocytic TLR activation and tolerance in COVID-19 patients; nucleic acid binding scavengers can counteract such TLR agonists

Ibtehaj Naqvi [a,1], Nicholas Giroux [b,c,1], Lyra Olson [c,d,2], Sarah Ahn Morrison [a,2], Telmo Llanga [c,2], Tolu O. Akinade [g], Yuefei Zhu [g], Yiling Zhong [g], Shree Bose [c,d], Stephanie Arvai [e], Karen Abramson [e], Lingye Chen [f], Loretta Que [f], Bryan Kraft [f], Xiling Shen [b], Jaewoo Lee [a], Kam W. Leong [g], Smita K. Nair [a,h,i,*], Bruce Sullenger [a,b,d,i,**]

[a] Duke University School of Medicine, Department of Surgery, Division of Surgical Sciences, USA
[b] Duke University, Department of Biomedical Engineering, Pratt School of Engineering, USA
[c] Duke University, Graduate School, USA
[d] Duke University School of Medicine, Department of Pharmacology and Cancer Biology, USA
[e] Duke University Center for Genomic and Computational Biology, RNA Sequencing Core, USA
[f] Duke University School of Medicine, Department of Medicine, Division of Pulmonary Medicine, USA
[g] Columbia University, Department of Biomedical Engineering, USA
[h] Duke University School of Medicine, Department of Pathology, USA
[i] Duke University School of Medicine, Department of Neurosurgery, USA

ARTICLE INFO

Keywords:
Major-biological sciences
Minor-immunology and inflammation

ABSTRACT

Millions of COVID-19 patients have succumbed to respiratory and systemic inflammation. Hyperstimulation of toll-like receptor (TLR) signaling is a key driver of immunopathology following infection by viruses. We found that severely ill COVID-19 patients in the Intensive Care Unit (ICU) display hallmarks of such hyper-stimulation with abundant agonists of nucleic acid-sensing TLRs present in their blood and lungs. These nucleic acid-containing Damage and Pathogen Associated Molecular Patterns (DAMPs/PAMPs) can be depleted using nucleic acid-binding microfibers to limit the patient samples' ability to hyperactivate such innate immune receptors. Single-cell RNA-sequencing revealed that $CD16^{+}$ monocytes from deceased but not recovered ICU patients exhibit a TLR-tolerant phenotype and a deficient anti-viral response after *ex vivo* TLR stimulation. Plasma proteomics confirmed such myeloid hyperactivation and revealed DAMP/PAMP carrier consumption in deceased patients. Treatment of these COVID-19 patient samples with MnO nanoparticles effectively neutralizes TLR activation by the abundant nucleic acid-containing DAMPs/PAMPs present in their lungs and blood. Finally, MnO nanoscavenger treatment limits the ability of DAMPs/PAMPs to induce TLR tolerance in monocytes. Thus, treatment with microfiber- or nanoparticle-based DAMP/PAMP scavengers may prove useful for limiting SARS-CoV-2 induced hyperinflammation, preventing monocytic TLR tolerance, and improving outcomes in severely ill COVID-19 patients.

1. Significance statement

Unfortunately, broadly effective therapeutic options for COVID-19 patients that require ICU-level care remain limited. To better understand the SARS-CoV-2 pathology, we studied blood and respiratory samples from COVID-19 ICU patients. We found that they suffered from an inflammatory storm stimulated by circulating molecules released by dead and dying cells called Damage and Pathogen

* Corresponding author. Duke University School of Medicine, Department of Surgery, Division of Surgical Sciences, USA.
** Corresponding author. Duke University, Department of Biomedical Engineering, Pratt School of Engineering, USA.
E-mail addresses: smita.nair@duke.edu (S.K. Nair), bruce.sullenger@duke.edu (B. Sullenger).
[1] These authors contributed equally (co-first authors).
[2] These authors contributed equally (co-second authors).

https://doi.org/10.1016/j.biomaterials.2022.121393
Received 14 January 2022; Accepted 24 January 2022
Available online 28 January 2022

Associated Molecular Patterns (DAMPs/PAMPs). We determined that nucleic acid binding microfibers can deplete such nucleic acid-containing DAMPs/PAMPs from patient samples. Moreover, we observed that prolonged, high levels of DAMPs/PAMPs hyperstimulate monocytes leading to their exhaustion in COVID-19 patients that succumb to the disease. Finally, we show that a nanoparticle-based DAMP/PAMP scavenger can neutralize such inflammatory agents present in critically ill patients and limit the ability of DAMPs/PAMPs to induce monocyte tolerance. Thus DAMP/PAMP scavengers represent therapeutic agents to potentially combat hyperinflammation and immune exhaustion in critically ill COVID-19 patients.

2. Introduction

Several groups have focused on characterizing and modulating hyperactive innate immune responses driven by sensing Damage- or Pathogen-Associated Molecular Patterns (DAMPs or PAMPs) released from dead and dying cells in a variety of disease types [1–3]. DAMPs and PAMPs are detected by pattern recognition receptors, such as Toll-like receptors (TLRs). TLRs are key innate immune sensors, several of which recognize nucleic acid-containing DAMPs/PAMPs to initiate signaling cascades and downstream immune responses [4,5]. TLR3 and TLR7/8 sense RNA, whereas TLR9 senses DNA and TLR4 senses DNA-protein complexes. Together, these nucleic acid-sensing TLRs are important mediators of the inflammatory response in cancer, autoimmune disease, and infection [5–8]. However, excessive activation of TLRs and their downstream signaling pathways via NFκB may contribute to the development and progression of lung injury and acute respiratory distress syndrome (ARDS) due to increased vascular permeability and lymphocyte and neutrophil activation [9,10]. We and others have previously shown that both the soluble and non-soluble fiber formulations of certain nucleic acid binding micro- and nano-materials can neutralize such DAMPs/PAMPs and prevent their activation of TLRs and downstream NFκB in models of lupus, rheumatoid arthritis, cancer, trauma, sepsis and influenza infection [11–22].

Infection by SARS-CoV-2 causes a broad spectrum of disease, from mild symptoms of upper respiratory infection to ARDS and respiratory failure requiring mechanical ventilation or extracorporeal membrane oxygenation [23–25]. Patients at the severe end of the disease spectrum, such as those in the intensive care unit (ICU), can quickly deteriorate and are at higher risk of mortality [23,25,26]. Underpinning these poor outcomes is a hyperinflammatory response in severely ill patients concurrent with a viral infection, which is associated with elevated levels of D-dimer, IL-6, lymphopenia, and neutrophilia among other laboratory abnormalities [24,26]. The TLR hyperstimulation we have studied and targeted with nano- and micro-materials in other disease types may be relevant to the hyperinflammatory response in COVID-19. Therefore, this study primarily focuses on characterizing TLR mediated inflammation in patients in the ICU with COVID-19 and exploring the ability of nucleic acid binding materials to mitigate the negative downstream consequences of nucleic acid-containing DAMPs/PAMPs on TLR hyperstimulation.

TLRs activated by DAMPs and PAMPs result in altered expression of cell surface receptors, cytokines, and chemokines. SARS-CoV-2 infection in ICU patients is associated with marked neutrophilia, with neutrophils also being a key source of DAMPs in this population of patients [27]. Some reports identified an increase in monocyte abundance associated with severe infection [28,29]. Monocytes and their subsets are key sensors of and responders to TLR mediated inflammation, especially following viral infection. Classical monocytes (i.e., $CD16^{-}CD14^{+}$ monocytes) typically represent the majority of circulating monocytes under healthy conditions (80–95% of total monocytes); intermediate ($CD16^{+}CD14^{+}$) and non-classical monocytes ($CD16^{+}CD14lo/-$) comprise the remaining 20-5% [30,31]. $CD16^{+}$ monocytes respond to TLR7/8-mediated inflammation, and $CD16^{-}$monocytes respond to TLR4-mediated inflammation [31]. The relationship between TLR-mediated inflammation and monocyte response in COVID-19 remains unexplored and is another focus of this study.

Under normal circumstances, TLR activation results in downstream signaling and gene transcription so that monocytes can respond to infection. However, severe infection and a hyperinflammatory environment can lead to hyperstimulation of TLRs and subsequent aberrant TLR downstream signaling. This persistent and aberrant downstream TLR signaling in the setting of hyperinflammation is referred to as TLR tolerance. TLR tolerance occurs when cells are repeatedly exposed to DAMPs and PAMPs, leading to an aberrant downstream immune response [15,32–36]. Under normal circumstances, the TLR signaling cascade activates NFκB and leads to a robust immune response. However, when immune cells, such as monocytes, are repeatedly exposed to TLR agonists, they become tolerant to further stimulation and cannot mount an effective response [15,32–36]. Previous studies have shown that monocytes isolated from patients with sepsis have reduced production of IL-10, IL-1β, and IL-12 in response to LPS treatment, regardless of patient survival [37]. However, when monocytes were isolated and activated with LPS later in the course of sepsis, monocytes from survivors regained the ability to produce these cytokines in response to LPS treatment, whereas monocytes from deceased patients did not recover. Moreover, this cytokine dysfunction could not be rescued with *in vitro* treatment of IFN-γ. This phenotype predisposes these patients to subsequent bacterial infections given the importance of IL-10, IL-1β, and IL-12 in the resolution of inflammation [37–40]. We, therefore, examined if monocytic TLR tolerance occurs in COVID-19 patients particularly in response to nucleic acid-containing DAMPs/PAMPs and whether nucleic acid binding nanomaterial-based therapies could mitigate TLR hyperactivation by patient samples and limit DAMP/PAMP-induced tolerance of monocytes.

To this end, we conducted longitudinal immune and DAMP/PAMP profiling of patients with COVID-19 requiring ICU-level care. We examined immune subsets in blood from critically ill COVID-19 patients using flow cytometry, reporter cell assays to measure TLR-activation potential, single-cell RNA-sequencing, and plasma proteomic profiling to assess differences between patients that survived versus those that did not. We observed a striking elevation of nucleic acid DAMPs/PAMPs in patients' lungs and blood and thus investigated the ability of nucleic acid-binding micro- and nanomaterials to neutralize the excessive DAMPs/PAMPs. We observe that such DAMP/PAMP scavenger treatment inhibits hyperinflammation and limits TLR tolerance suggesting that such materials may prove useful for improving outcomes of severely ill COVID -19 patients.

3. Results

3.1. Immune profiling of COVID-19 ICU patient blood reveals distinct monocyte subsets associated with clinical outcome

Fresh whole blood was collected from patients at time points indicated and analyzed as described in methods. Flow cytometry results support the trends observed in previous reports [23,24,41–47], including lymphopenia and neutrophilia in most patients, regardless of treatment with dexamethasone or clinical outcome (Fig. 1A–G). When comparing patient groups by dexamethasone treatment and clinical outcomes, no significant differences were observed in the frequency of CD4 and CD8 T cells, NKT cells, NK cells, basophils, or eosinophils (Fig. 1B–I) in the periphery. We observed that a subset of patients had elevated percentages of monocytes while other patients had percentages within the normal range (Fig. 1J). This prompted us to further examine this subset of cells and the canonical subpopulations of monocytes.

Monocyte subsets are categorized by surface expression of CD16 and CD14. Monocytes that expressed CD16, either classified as intermediate monocytes ($CD16^{+}CD14^{+}$) or non-classical monocytes ($CD16^{+}CD14lo/-$), were annotated as $CD16^{+}$ monocytes [30,31]. Dexamethasone-naïve ICU patients that recovered from infection were distinguishable from

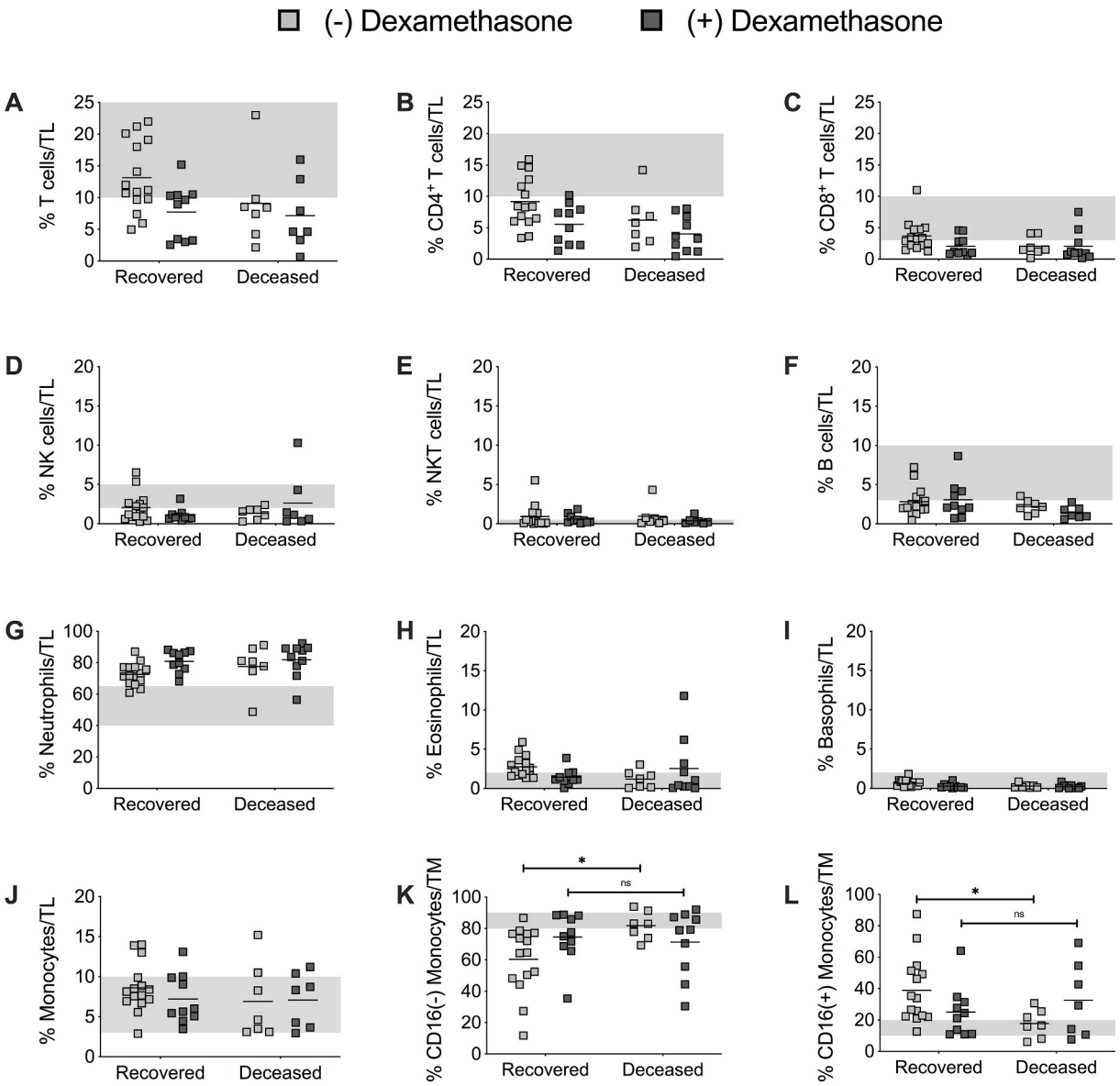

Fig. 1. Immune cell subset profiling in the blood of recovered versus deceased COVID-19 patients in the ICU with and without dexamethasone. Data for immune cell subsets are presented as a percentage of total leukocytes (TL) or total monocytes (TM) on the last day of study. Gray shaded area shows the normal range for each immune cell subset. **A.** $CD3^+$ T cell percentages are consistent with lymphopenia regardless of clinical status; (+) dexamethasone trends lower than (−) dexamethasone. **B.** $CD4^+$ T cell percentages are consistent with total T cells. **C.** $CD8^+$ T cell percentages are consistent with $CD4^+$ T cells and total T cells. **D.** NK cell percentages are below normal range regardless of clinical or dexamethasone status. **E.** NKT cell percentages are higher than normal in (−) dexamethasone patients regardless of clinical status. (+) dexamethasone patients have NKT cell percentages closer to the normal range with discharged patients trending higher than deceased patients. **F.** B cell percentages are below normal ranges regardless of clinical or dexamethasone status. **G.** Neutrophil percentages are above normal ranges regardless of clinical or dexamethasone status. **H.** Amongst recovered patients, eosinophils are higher than normal in (−) dexamethasone and within the normal range in (+) dexamethasone; this pattern is reversed amongst deceased patients. **I.** Basophil percentages are within normal range regardless of clinical or dexamethasone status. **J.** Total monocyte percentages are within normal range regardless of clinical or dexamethasone status. **K.** CD16 (−) monocyte percentages trend lower in (−) dexamethasone patients that were discharged versus those that died while CD16 (−) monocyte percentages were roughly equivalent in (+) dexamethasone patients regardless of clinical outcome. **L.** CD16 (+) monocyte percentages are significantly higher in (−) dexamethasone patients that were discharged versus those that died while CD16 (+) monocyte percentages were roughly equivalent in (+) dexamethasone patients regardless of clinical outcome. * = $p < 0.05$, ns = not significant via 2-tailed *t*-test; no statistically significant differences were noticed unless indicated in the figure.

deceased patients based on the abundance of $CD16^+$ monocytes (Fig. 1J-L). Patients who were dexamethasone-naive and recovered from infection had higher levels of $CD16^+$ monocytes. Recovery was defined as discharge from the hospital or transition out of the ICU. In contrast, deceased patients had lower levels of $CD16^+$ monocytes, and $CD16^-$monocytes were the pre-dominant monocyte population in the periphery of these patients. The association between $CD16^+$ monocyte abundance and positive clinical outcome in patients treated with dexamethasone was not statistically significant, exemplifying the potent immune-modulatory effects of dexamethasone. To interrogate the effect of COVID-19 on nascent monocyte function directly, we analyzed samples from the ICU COVID-19 patient cohort that was dexamethasone-naive. Regardless of the difference in $CD16^+$ cells which are known to be particularly sensitive to TLR7/8 activation by RNA-based DAMPs/PAMPs encouraged us to evaluate the levels of such inflammatory nucleic acids in patient samples.

3.2. Longitudinal profiling of serum and endotracheal aspirate (ETA) from COVID-19 ICU patients reveals elevated levels of DAMPs and PAMPs that potently activate nucleic acid-sensing TLR signaling

To investigate the association between $CD16^{+}$ monocytes, TLR activation and clinical outcome, we analyzed blood, plasma, and endotracheal aspirate (ETA) from ICU COVID-19 patients for TLR agonists. Among the four TLRs tested, TLR3 and TLR7 showed the most consistent activation by serum across all patients and all time points when compared to healthy control (Fig. 2A). Since TLR3 and TLR7 are sensors for double-stranded and single-stranded RNA, respectively, we concluded that serum samples from our COVID-19 ICU cohort have elevated levels of pro-inflammatory RNA molecules, consistent with the fact that SARS-CoV-2 is an RNA virus. TLR4 and TLR9 were also activated by serum from COVID-19 ICU patients, though the level of activation was not as high as found with TLR3 and TLR7, particularly when viewed longitudinally (Fig. 2A). TLR4 and TLR9 are sensors of lipopolysaccharide (LPS) and bacterial DNA, respectively. TLR4 and TLR9 are also activated by endogenous molecules released during cell death such as nucleosomes, HMGB-1, and mitochondrial DNA [48]. We also characterized the TLR profile of ETA from 10 COVID-19 ICU patients. For each TLR tested, ETA produced a 3-4-fold higher activation than serum from 72 COVID-19 patients (Fig. 2B). These data further highlight the respiratory localization of the inflammatory syndrome in patients critically ill with COVID-19. These results indicate that the airway remains a major location of DAMP/PAMP generation and hyperinflammation in these patients characterized by high levels of inflammatory agonists that activate nucleic acid-sensing TLRs particularly the RNA sensors TLR3 and TLR7/8 which are on $CD16^{+}$ monocytes.

3.3. Nucleic acid-binding microfibers can deplete DAMPs/PAMPs from COVID-19 ICU patient serum and ETA and limit their ability to stimulate TLRs and induce downstream NFκB activation

The observation that nucleic acid-containing DAMPs/PAMPs are abundant in COVID-19 ICU patient samples led us to explore if such TLR agonists can be depleted using a nucleic acid-scavenging microfiber mesh. Previously we observed that such microfibers could effectively remove DAMPs present in the blood of trauma patient samples and limit such patient samples from stimulating TLRs [15]. Electrospun PSMA/-polystyrene microfibers (average diameter 2.5 ± 0.1 μM) were generated and PEI and PAMAM-G3 were conjugated onto the PSMA/polystyrene mesh as previously described [15]. Treatment of patient samples with these nucleic acid-binding microfibers dramatically decreased the activation of TLR3, TLR4, TLR7, and TLR9 by serum and ETA from COVID-19 patients. As shown in Fig. 3, the level of inhibition achieved is essentially complete, reducing levels of TLR activation to those observed with media alone (Fig. 3A–H). Thus, treatment with this nucleic acid-binding microfiber mesh neutralized DAMPs and PAMPs and prevented NFκB activation by depleting these TLR agonists from serum and ETA samples collected from blood and lungs of critically ill COVID-19 patients.

We also quantified the ability of the nucleic acid-scavenging fibers to deplete DAMPs/PAMPs from patient samples. We found that treatment with the fibers was able to significantly deplete DNA, RNA, HMGB-1, and nucleosomes from both serum and ETA of COVID-19 patient samples (Fig. 3I-P). DNA and HMGB-1 are potent endogenous activators of TLR9 [49]. RNA is a canonical activator of TLR3 and TLR7. HMGB-1 and nucleosomes also potently activate TLR4. We also measured human serum albumin as a non-inflammatory protein control. Though albumin carries a net negative charge, the depletion effect by the nucleic acid-binding fiber is modest in serum and non-existent in ETA (Fig. 3Q, R). These data demonstrate that nucleic acid-containing DAMP/PAMP scavenger fibers can deplete a diverse array of pro-inflammatory

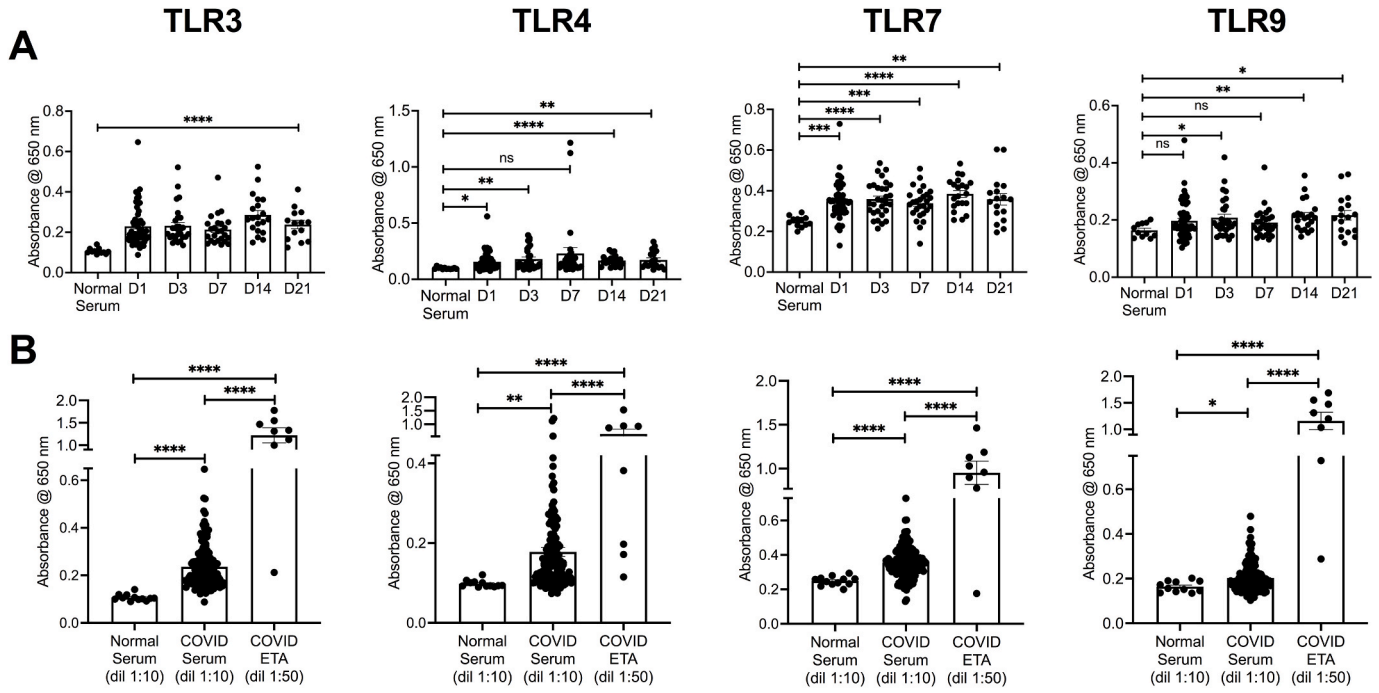

Fig. 2. Longitudinal TLR activation profiling of serum and ETA from ICU patients with COVID-19 using HEK-TLR reporter cells for TLRs 3, 4, 7 and 9. **A.** Longitudinal profiling of TLR3, TLR4, TLR7 and TLR9 activation using COVID-19 patient serum shows the following: 1] strong activation of TLR3 and TLR7 by serum across all timepoints; 2] activation of TLR4 by serum on days (D) 1, 3, 14 and 21; 4] activation of TLR9 by serum on days (D) 3, 14 and 21. **B.** COVID-19 patient serum and ETA significantly activate TLR3, TLR4, TLR7 and TLR9 compared to normal serum. * = $p < 0.05$ via 2-tailed *t*-test; *** = $p < 0.001$ via 2-tailed *t*-test; **** = $p < 0.0001$ via 2-tailed *t*-test; ns = not significant via 2-tailed *t*-test; D = day; dil = dilution.

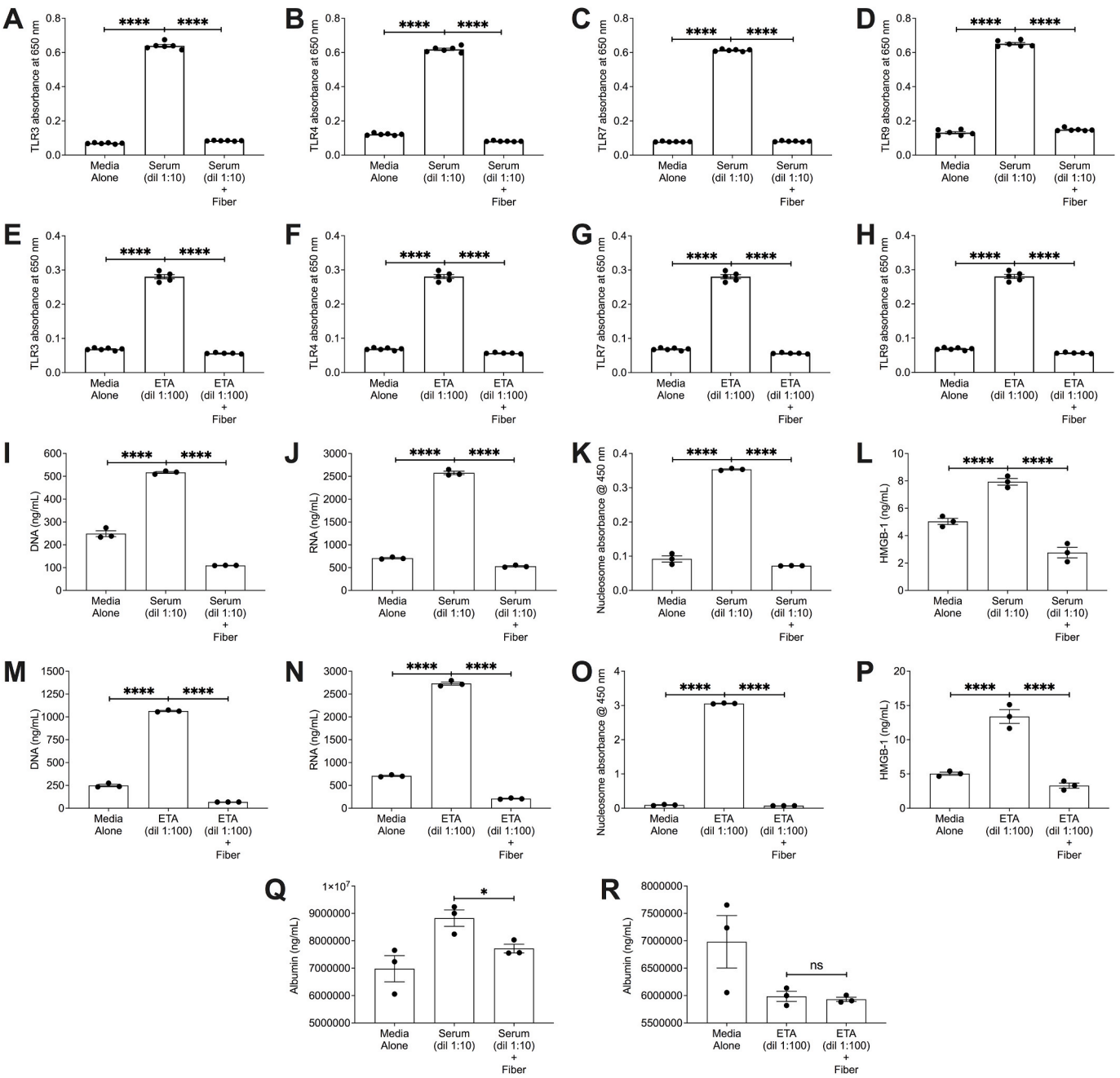

Fig. 3. Treatment of serum and endotracheal aspirate (ETA) from COVID-19 ICU patients with nucleic acid-binding microfibers reduces the activity and quantity of TLR activating DAMPs/PAMPs. Treatment of serum with nucleic acid binding fiber significantly reduces TLR activation of HEK-TLR reporter cells for TLRs 3, 4, 7 and 9. **A.** TLR-3; **B.** TLR-4; **C.** TLR-7; **D.** TLR-9. Treatment of ETA with nucleic acid binding fiber significantly reduces TLR activation of HEK-TLR reporter cells for TLRs 3, 4, 7 and 9. **E.** TLR-3; **F.** TLR-4; **G.** TLR-7; **H.** TLR-9. Treatment of serum with nucleic acid binding fiber significantly reduces levels of **I.** DNA; **J.** RNA; **K.** nucleosome; **L.** HMGB-1. Treatment of ETA with nucleic acid binding fiber significantly reduces levels of **M.** DNA; **N.** RNA; **O.** nucleosome; **P.** HMGB-1. **Q.** Treatment of serum with nucleic acid binding fiber modestly reduces albumin levels. **R.** Treatment of ETA with nucleic acid binding fiber has no effect on albumin levels. * = $p < 0.05$ via 2-tailed *t*-test; *** = $p < 0.001$ via 2-tailed *t*-test; **** = $p < 0.0001$ via 2-tailed *t*-test; NS = not significant via 2-tailed *t*-test.

molecules present in COVID-19 patient samples while having only a modest effect on a control protein and suggest that such fibers may be useful for depleting DAMPs/PAMPs from COVID-19 patients requiring life-saving, supportive care such as extracorporeal membrane oxygenation (ECMO).

3.4. Single-cell RNA sequencing of COVID-19 patient monocytes reveals phenotypic differences and DAMP/PAMP response patterns specific for clinical outcome

Next, we sought to explore the functional connection between the elevated levels of TLR activating DAMPs and PAMPs and $CD16^+$ monocyte populations in COVID-19 ICU patients with different clinical outcomes. We conducted single-cell RNA-sequencing and quantified the transcriptional response to activation with TLR agonists in monocytes from COVID-19 ICU patients. Monocytes were treated with media, LPS

(TLR4 agonist and positive control for PAMP activation), or R848 (TLR7/8 agonist and mimic of viral RNA PAMP and the high levels of TLR7/8 agonists present in patients' lungs and blood). Following sequencing, we annotated four distinct monocyte populations by cell type and clinical outcome: CD16$^-$monocytes and CD16$^+$ monocytes isolated from either recovered or deceased patients (Fig. 4A, S1A-C). Samples treated with TLR agonists LPS or R848 clustered separately according to clinical outcome following dimensionality reduction (Fig. 4B). In the media-treated baseline samples, the clusters did not separate. These results support the hypothesis that functional differences in monocytes from COVID-19 patients with differential clinical outcomes contribute to dysregulation of TLR-mediated anti-viral immunity.

We found no differential gene expression between CD16$^-$monocytes

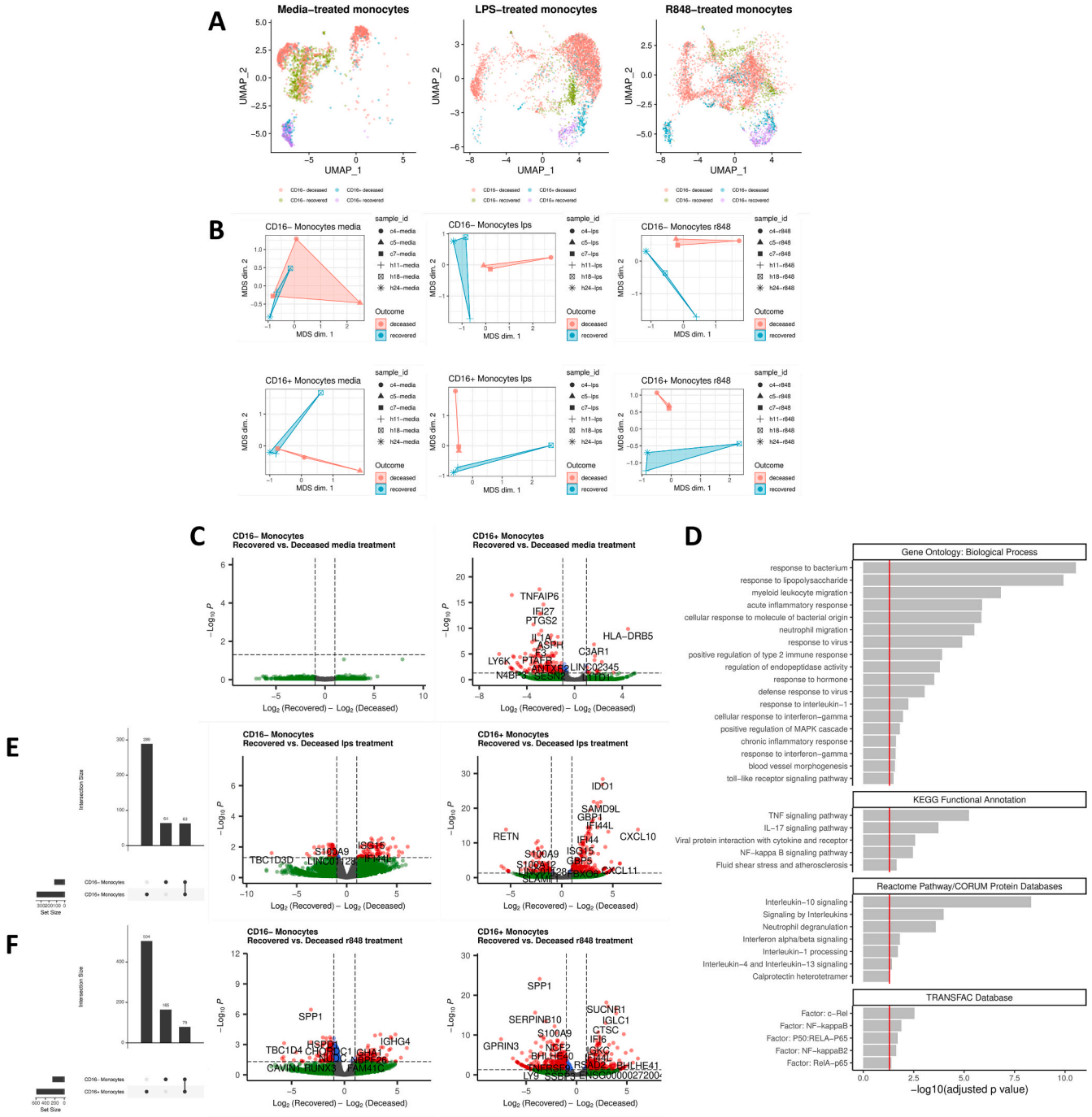

Fig. 4. Differential gene expression in monocytes from subjects with divergent outcomes. Monocytes isolated from blood obtained from COVID-19 patients (n = 3 for each group, recovered and deceased) were treated with media, LPS, or R848. **A.** UMAP projection of monocytes collected from subjects with COVID-19 and treated with media, LPS, or R848. UMAPs are colored by cell type and subject outcome. **B.** MDS ordination plot of either CD16$^-$monocytes (top) or CD16$^+$ monocytes (bottom) from samples treated with media, LPS, or R848. **C.** Differential expression of media-treated monocytes from recovered or deceased COVID-19 patients. Statistical significance is defined as $q < 0.05$ and log2FC > 1. **D.** Functional enrichment analysis of genes with elevated expression in CD16$^+$ monocytes from deceased subjects relative to recovered subjects. **E.** Differential expression of LPS-treated monocytes and **F.** R848-treated monocytes from recovered or deceased COVID-19 patients. Intersections between differentially expressed gene sets are plotted as UpSet plots (left). Statistical significance is defined as $q < 0.05$ and log2FC > 1.

isolated from recovered (n = 3) or deceased patients (n = 3) (Fig. 4C). In contrast, we observed that CD16$^+$ monocytes from deceased patients had a transcriptional profile consistent with hyper-inflammatory activation, characterized by elevated expression of interleukin-1α (IL1A), interferon-stimulated gene IFI27, and TNFAIP6 at this baseline condition (without additional stimulation). CD16$^+$ monocytes from recovered patients had higher expression of genes related to adaptive immunity, including HLA-DRB5. Functional enrichment analysis applied to these differentially expressed genes revealed that CD16$^+$ monocytes from deceased patients were enriched in the tumor necrosis factor (TNF-α), IL-17, and IL-10 signaling pathways, consistent with the immunopathology of COVID-19 in critically ill patients (Fig. 4D). Additionally, we identified enrichment of myeloid and neutrophil activation pathways and NFκB transcription factor (TF) motifs in genes with higher

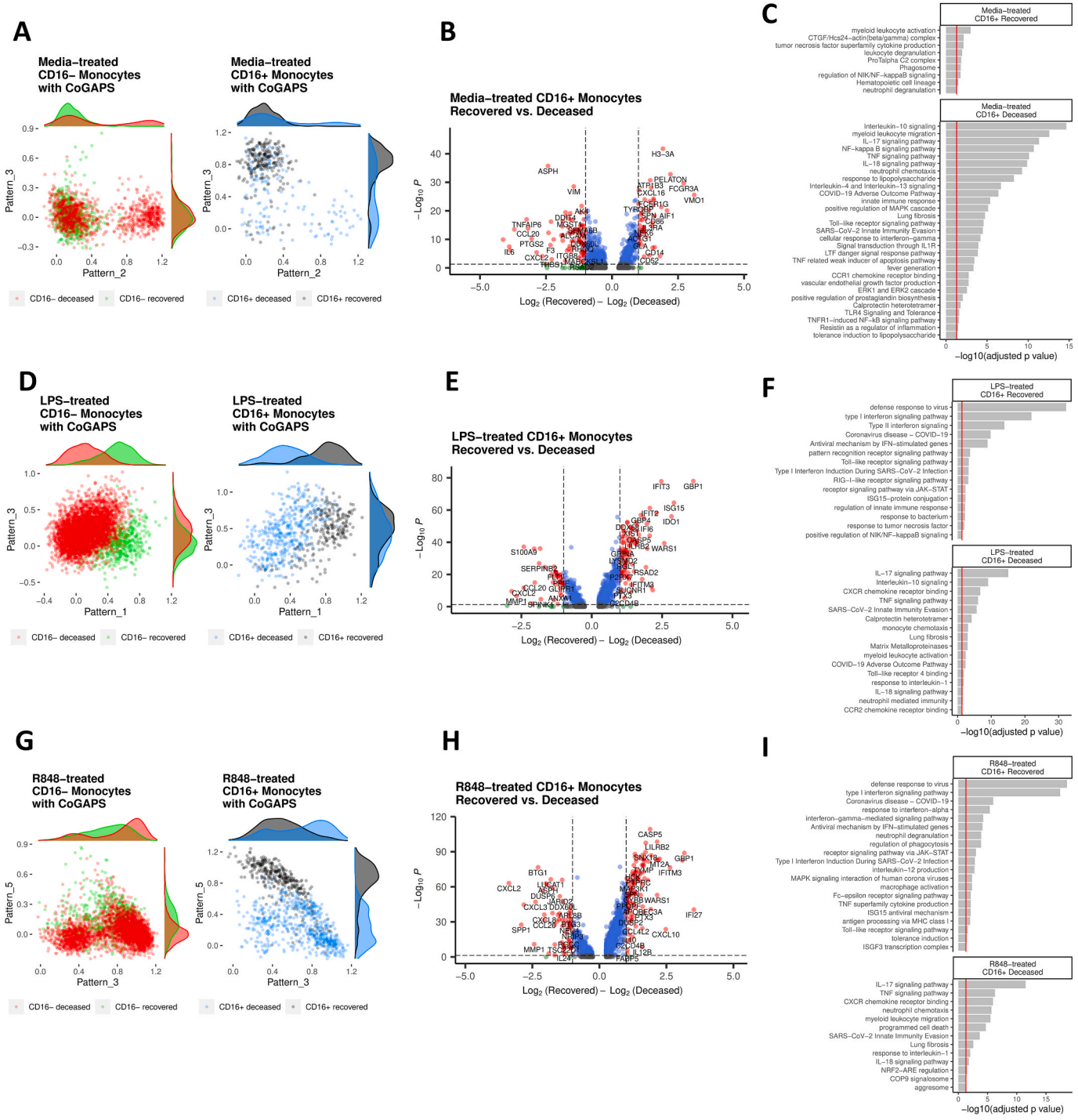

Fig. 5. Immune tolerance signatures in CD16$^+$ monocytes from deceased subjects. **A.** Scatter plot of CoGAPS pattern scores for media-treated CD16$^-$monocytes (left) and CD16$^+$ monocytes (right). **B.** Differential gene expression markers and **C.** Functional enrichment analysis of CD16$^+$ monocytes with pattern 3 score >0.5 compared to all other CD16$^+$ monocytes. **D.** Scatter plot of CoGAPS pattern scores for LPS-treated CD16$^-$monocytes (left) and CD16$^+$ monocytes (right). **E.** Differential gene expression markers and **F.** Functional enrichment analysis of CD16$^+$ monocytes with pattern 1 score >0.7 compared to all other CD16$^+$ monocytes. **G.** Scatter plot of CoGAPS pattern scores for R848-treated CD16$^-$monocytes (left) and CD16$^+$ monocytes (right). **H.** Differential gene expression markers and **I.** functional enrichment analysis of CD16$^+$ monocytes with pattern 5 score >0.6 compared to all other CD16$^+$ monocytes.

expression in CD16$^+$ monocytes from deceased patients.

Stimulated monocytes treated with LPS or R848 were characterized by distinct gene expression profiles that reflected clinical outcome. CD16$^+$ monocytes from deceased patients stimulated with LPS express markers of significant immune dysfunction compared to recovered patients (Fig. 4E). Recovered patients' cells expressed markers of interferon-mediated antiviral immunity, including the genes IFI44, IFI44L, and ISG15, as well as chemokine ligands CXCL10 and CXCL11 associated with immune infiltration in the airways while deceased patients' monocytes did not [50]. Similar dysfunction was observed in CD16$^+$ monocytes stimulated with R848, marked by expression of inflammatory macrophage- and neutrophil-associated genes SPP1 and NCF2 only in cells from deceased patients [51,52]. Overall, the number of differentially expressed genes in CD16$^+$ monocytes was consistently larger than the number of differentially expressed genes in CD16$^-$monocytes. This observation supports the hypothesis that CD16$^+$ monocytes are key regulators of COVID-19 immunopathology and harbor biomarkers associated with clinical outcomes.

The transcriptomic profiles of monocytes isolated from deceased patients and treated with TLR agonists reveal a phenotype consistent with monocyte tolerance, a process that can be engendered by repeated exposure to inflammatory mediators such as those seen in ICU patients with COVID-19 [53]. Specifically, we found that CD16$^+$ monocytes from deceased patients treated with either media or TLR agonists expressed similar levels of S100A8/9 (circulating calprotectin) and SIGLEC9, a protein that regulates LPS-mediated induction of tolerance via CCR7 (Fig. S1D) [54–56]. This expression pattern was not observed in CD16$^+$ monocytes from recovered patients (Fig. S1D).

To further explore this connection, we performed non-negative matrix factorization on single-cell gene count matrices to identify patterns of correlated gene expression associated with clinical outcomes. CD16$^+$ monocytes, not treated with a TLR agonist, from recovered subjects were characterized by high expression of pattern 3 (Fig. 5A right, S2A-B). In contrast, a sub-population of media-treated CD16$^+$ monocytes from deceased subjects have low expression of pattern 3 (Fig. 5A right), suggesting that these cells lack functional activity otherwise observed in recovered patients with a competent immune response. Next expression pattern 3 was used to stratify CD16$^+$ monocytes from recovered or deceased patients (Fig. 5B). Genes with higher expression in deceased subjects were enriched in IL-17, IL-10, and NFκB signaling pathways (Fig. 5C). Additionally, we identified markers of neutrophil chemotaxis and innate immunity evasion in the deceased patients, which were not present in recovered patients. Overall, these data indicate that CD16$^+$ monocytes from deceased but not recovered patients exhibit hallmarks of TLR tolerance.

To explore this TLR tolerance phenotype further, similar analyses were applied to monocytes treated with the TLR agonists, LPS or R848. LPS-treated monocytes were stratified into two populations based on the expression of genes in pattern 1 (Fig. 5D, S2C-D). Monocytes from recovered patients were observed to have high expression of pattern 1 genes, whereas cells from deceased patients had low expression of pattern 1 genes. These monocyte populations were used to identify enriched gene expression in either recovered or deceased patients (Fig. 5E). CD16$^+$ monocytes from deceased subjects had higher expression of the alarmin protein S100A9 and T cell chemoattractants CXCL10 and CXCL11, and recovered subjects had higher expression of interferon-response genes, including IFIT2, IFIT3, and ISG15. The differential gene expression profiles identified in recovered patients were enriched in interferon and RIG-I-like receptor signaling pathways (Fig. 5F). R848-treated monocytes were stratified into two populations based on the expression of pattern 5 genes (Fig. 5G, S2E-F). Monocytes from recovered patients expressed higher levels of pattern 5 than monocytes from deceased patients. Differential gene expression profiles in CD16$^+$ monocytes associated with clinical outcome identified activation of macrophages and the JAK-STAT signaling pathway in recovered patients (Fig. 5H–I). Pathway enrichment in CD16$^+$ monocytes from deceased patients identified cytokine signaling by IL-17 and TNF-α. Thus, gene expression in monocytes stimulated with LPS or R848 from deceased patients suggests a non-productive response.

3.5. Monocyte gene network analyses distinguish TLR activation responses associated with ICU patient outcome

We then performed gene regulatory network analysis to understand which transcription factors coordinate differential gene expression in CD16$^+$ monocytes. Regulon activity was inferred from genes with differential expression between CD16$^+$ monocytes from recovered versus deceased patients. Media alone-treated CD16$^+$ monocytes from recovered patients were enriched in EGR3 and JUND regulon activity, two proteins required to activate the AP-1 transcription factor, which broadly regulates anti-viral immunity (Fig. 6A) [57,58]. After stimulation with either LPS or R848, CD16$^+$ monocytes from recovered patients were consistently enriched in STAT1, STAT2, and STAT4 regulon activity (Fig. 6B–C). STAT protein expression is required to restrict viral infection via induction of interferon signaling [59]. In contrast, CEBPB and ATF4 regulon activity was decreased in R848-treated CD16$^+$ monocytes from recovered patients. The induction of ATF4 activity by TLR4 signaling interacts with CEBPB to regulate the production of inflammatory cytokines including IL-6, IL-8, and TNF-α [60,61]. The NFκB pathway is known to play a critical role in downstream signaling after TLR activation [62–65]. Indeed, we identified pathway-level enrichment of NFκB signaling associated with CD16$^+$ monocytes from deceased patients at the baseline, media-treatment condition (Fig. 6D). After stimulation with TLR agonists, recovered patients expressed genes regulated by NFκB at a higher level while such gene expression in monocytes from deceased patients was unchanged with stimulation (Fig. 6E–F). In summary, media-treated monocytes from deceased patients had elevated baseline expression of the NFκB pathway compared to recovered patients. We found a consistent negative correlation between expression of the NFκB inhibitor, NFKBIA, and JUND in CD16$^+$ monocytes from deceased patients (Fig. 6G–I). At baseline, monocytes from recovered patients expressed high levels of JUND, and monocytes from deceased patients expressed high levels of NFKBIA instead. Following stimulation with LPS or R848, CD16$^+$ monocytes from recovered patients expressed both JUND and NFKBIA, whereas co-expression of these genes was not observed in deceased patients, suggesting that JUND expression is a compensatory response to hyperstimulation of the NFκB pathway [66]. Taken together with our DAMP/PAMP profiling studies, these results suggest that the high levels of nucleic acid-containing DAMPs/PAMPs present in patients may lead to immune tolerance in ICU patients that succumb to COVID-19.

3.6. Longitudinal proteomics reveals markers of heightened myeloid activation and consumption of PAMP carrier proteins in deceased patients

For further validation of the differential transcription expression and functional observations from our RNA-sequencing data, we performed an unbiased proteomics analysis on plasma from four different ICU patients that recovered from COVID-19 and four different patients that did not.

We identified similarities between the circulating proteome from these four deceased patients and the transcriptomic profiles of isolated monocytes from three different deceased patients. Functional pathway analysis performed on the plasma proteome demonstrated an enrichment of biological processes related to myeloid activation, recruitment, and migration in deceased patients relative to survivors (Fig. 7A). Specifically, clustering performed on these proteomic data identified markers of mucosal innate immunity, antibacterial response, and cellular response to lipopolysaccharide in deceased patients. Furthermore, the proteinaceous markers enriched in deceased patients over recovered patients indicated heightened myeloid activity (Fig. 7B).

Next we compared longitudinal samples from both recovered and

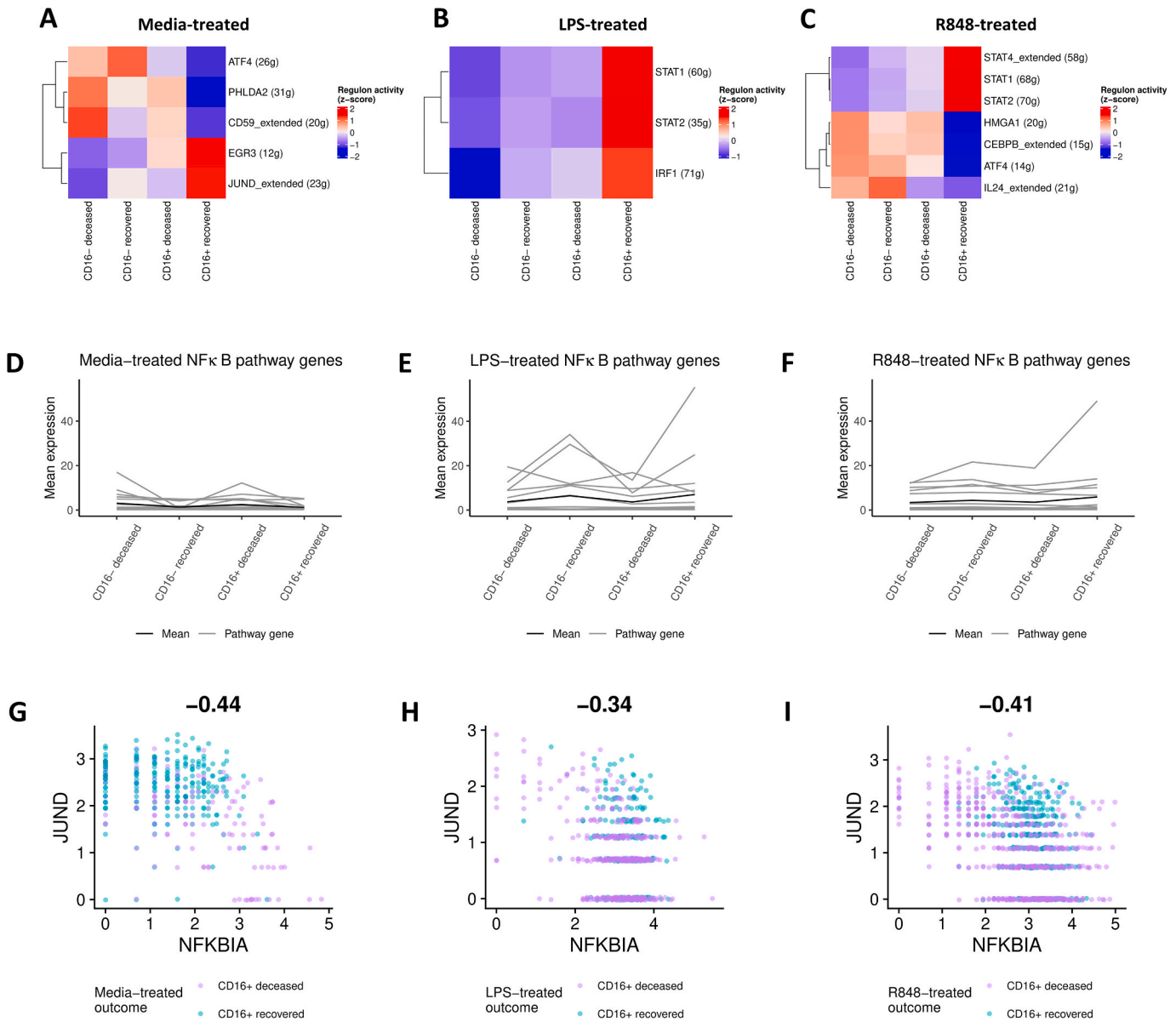

Fig. 6. Gene regulatory network dynamics between monocyte populations. Heatmap of transcription factor regulon activity for **A.** media alone-treated, **B.** LPS-treated, or **C.** R848-treated monocytes from subjects with divergent outcomes. Regulons were identified from genes differentially expressed between CD16^{+} monocytes from recovered and deceased subjects. Z-scores are used for visualization to compare across cell types and outcome groups. **D.** Average gene expression for genes in the NF-kB signaling pathway across media-treated, **E.** LPS-treated, or **F.** R848-treated monocyte populations collected from subjects who recovered or died from COVID-19. **G.** Scatter plot of NFKBIA and JUND expression in media-treated, **H.** LPS-treated, or **I.** R848-treated CD16^{+} monocytes from subjects with divergent outcomes. The correlation between NFKBIA and JUND expression is given for each plot.

deceased patients (Fig. 7C). We observed that deceased patients had higher circulating levels of proteins secreted by activated neutrophils, including NGAL, PRTN3, MMP9, MPO, TRFL, and DEF1 [67]. These proteins are secreted by neutrophils in response to microbial-induced inflammation and are mediated by TLR signaling (Fig. 7C) [67–71]. Additionally, levels of S100A9, an alarmin protein, were also elevated in deceased patients compared to recovered patients (Fig. 7C) [48,72]. S100 proteins are markers of inflammation involved with positive feedback of TLR4 expression [48,72]. These data are consistent with the monocyte RNA sequencing data, which showed that anti-microbial pathways are elevated in cells from deceased patients compared to recovered patients.

We also identified proteins with higher levels in recovered patients compared to deceased patients. For example, MARCO, a scavenger receptor expressed by macrophages that binds PAMPs in circulation and activates TLR signaling [73,74], is significantly lower in deceased patients relative to recovered patients (Fig. 7C). These findings suggest that PAMP binding and delivery to TLRs is consuming MARCO in deceased patients (Fig. 7C,E). A similar pattern was observed for various apolipoproteins, including APOA1, APOA2, APOH (Fig. 7C,E) as well as APOD and APOC4 (Fig. S3), which have reduced levels in plasma from deceased patients compared to recovered patients (Fig. 7C–E). Apolipoproteins act as carriers for PAMPs to activate TLR signaling and facilitate anti-viral immunity [75–77]. The proteomic evidence that free MARCO and apolipoproteins are decreased, and apparently being consumed, in deceased patient blood is consistent with the transcriptomic findings that monocytes from deceased patients have increased activation of TLRs.

Collectively, the COVID-19 ICU patient DAMP/PAMP TLR reporter cell activation studies, single-cell RNA sequencing, and proteomics

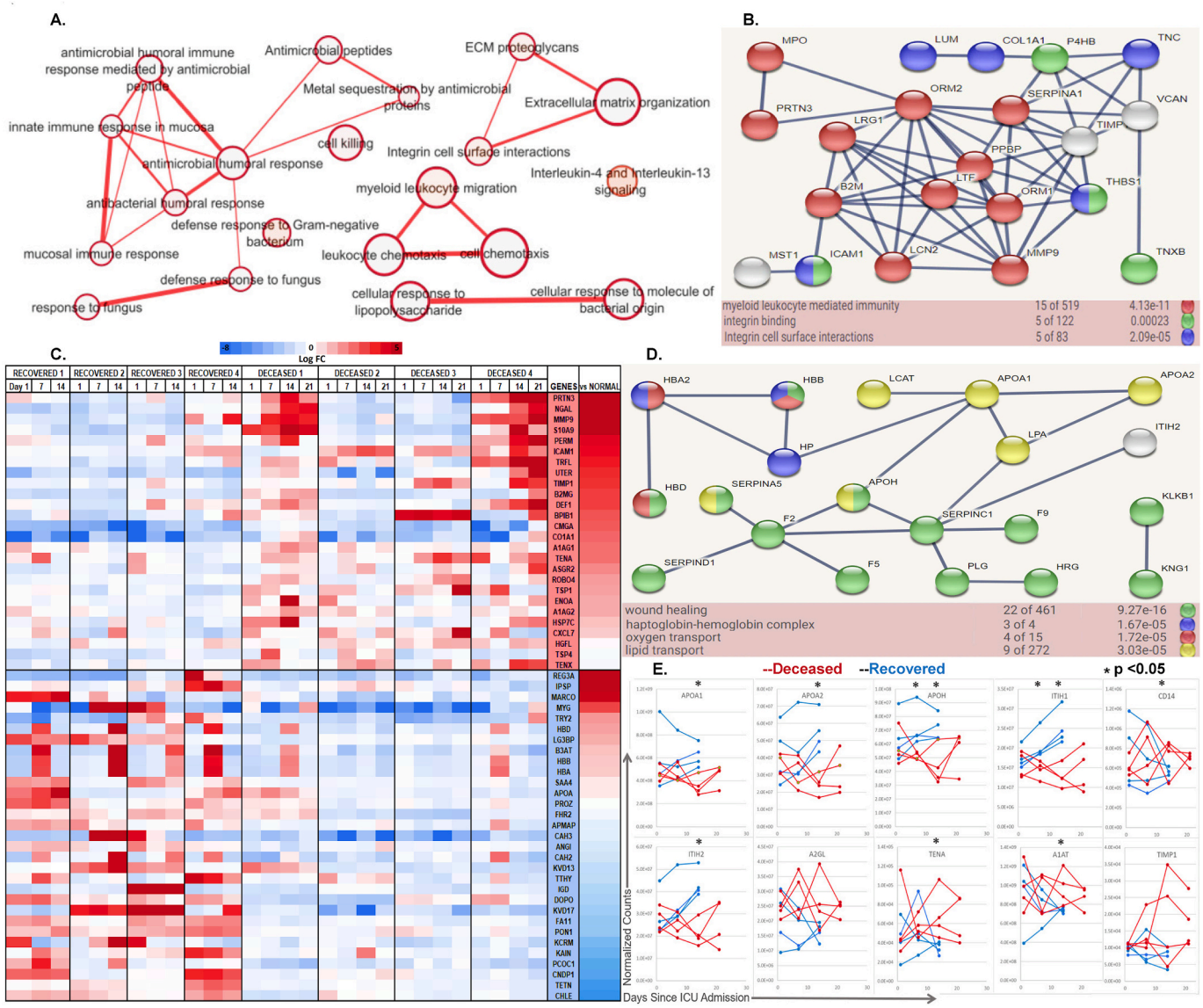

Fig. 7. Myeloid activation and PAMP carrier consumption in deceased patients using proteomics. A. Significant pathway (adjusted $p < 0.05$) similarity clustering of differentially upregulated proteome in deceased patients relative to survivors **B.** High confidence (>0.9 Confidence) STRING network of myeloid related immune interactions of differentially upregulated proteome and their dominating pathways **C.** Expression heatmap for immune-related differentially upregulated (red) and downregulated (blue) proteins over time relative to the average value for all infected patients, ordered by their levels compared to uninfected controls (right bar). **D.** High confidence (>0.9 Confidence) STRING network for protein interactions of differentially downregulated proteome and dominating pathways. **E.** Time-series plots for differentially expressed protein hits with trending and significant timepoint values.

analyses indicate that TLR hyperstimulation by nucleic acid-containing DAMPs/PAMPs can lead to excessive monocyte activation and consumption of immune modulators, all of which are associated with poor outcomes for COVID-19 ICU patients. Therefore, we next investigated whether DAMP/PAMP nanoscavengers can limit such TLR hyperactivation and TLR tolerance in monocytes.

3.7. MnO-based nanoparticles mitigate TLR stimulation by COVID-19 ICU patient serum and ETA, and prevent DAMP/PAMP-mediated induction of TLR tolerance in monocytes

The observation that nucleic acid-binding microfibers can capture and neutralize DAMPs/PAMPs (Fig. 3) led us to evaluate whether a soluble nanoparticle could be identified to counteract DAMPs/PAMPs in COVID-19 patient samples. To this end, we evaluated a new, soluble form of a nucleic acid binding nanoparticle-based upon manganese oxide (MnO). Given the uncharacterized nature of this MnO nanomaterial, we first assessed its fundamental properties. After synthesis, we determined that the MnO particles generated ranged in size from 30 to 100 nm and have a zeta potential is about −20 mV. We have evaluated the calf thymus DNA binding affinity of the manganese oxide nanomaterials (MnO NPs) in Tris-EDTA (TE) buffer by measuring unbound PicoGreen-labeled DNA. Despite their net negative surface charge, MnO NPs exhibit high DNA binding affinity (Fig. S4B), which is comparable to the nucleic acid binding polymer (PAMAM-G3) and has reduced cell toxicity compared to PAMAM-G3 (Fig. S4A). Next, we evaluated the nucleic acid scavenging activity of the MnO nanoparticles using TLR reporter cells. The MnO NPs inhibit CpG-induced activation of HEK-Blue hTLR9 cells, inhibit poly (I:C)-induced activation of HEK-Blue hTLR3 cells, and ORN06/LyoVec (ORN)-induced activation of HEK-Blue hTLR8 cells in a dose-dependent manner, regardless of the presence or absence of FBS (Fig. 8). The MnO-based nanoparticle has several distinct advantages when compared to other soluble nucleic acid binding nanomaterials we have previously tested. First, MnO nanoparticles

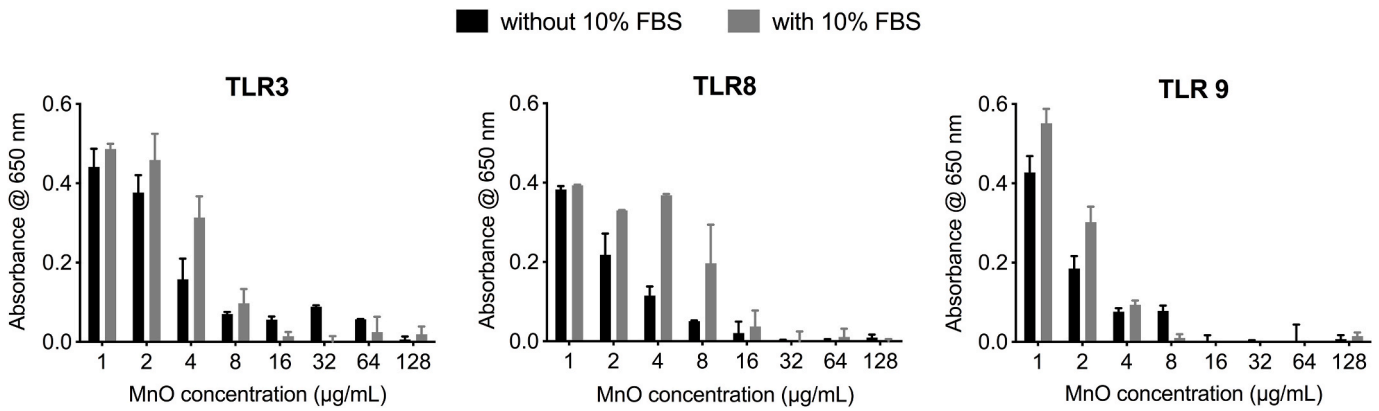

Fig. 8. MnO nanoparticles inhibit agonist mediated TLR activation. MnO inhibits activation of HEK-Blue hTLR3 (left), hTLR8 (middle), hTLR9 (right) cells in the absence or presence of FBS after nanomaterial treatment for 24 h in a dose-dependent manner. Experiments were repeated (N = 3). Data are presented as bars ± SEM. All agonists were purchased from Invivogen. ORN refers to ORN06/LyoVec.

maintain a potent ability to bind to inflammatory nucleic acids with a significantly improved toxicity profile when compared to other polymers (Fig. 8). Second, MnO nanoparticles are biodegradable and therefore are not expected to display the same level of toxicity to clearance organs observed with other classes of nucleic acid-binding nanomaterials such as the polyamidoamine or PAMAM family of polymers.

Given these advantages, we wanted to test the utility of such MnO nanoparticles in controlling TLR stimulation by COVID-19 ICU patient samples. As shown in Fig. 9, MnO nanoparticle addition significantly reduced stimulation of TLR 3, 4, 7 and 9 by the DAMPs/PAMPs present in COVID-19 ICU patient serum and ETA (Fig. 9A and B). The level of inhibition achieved with the nanoparticle scavengers is essentially 100% and comparable to that achieved using the microfiber DAMP/PAMP scavenger (compare Figs. 3 and 9). Next, we investigated whether mitigation of TLR stimulation by MnO nanoparticle could prevent induction of TLR tolerance in monocytes *ex vivo*. To this end, we conducted an experiment in which freshly isolated primary human monocytes were treated with Poly I:C (double-stranded viral RNA PAMP mimic that activates TLR3) for 24 h, followed by treatment with LPS (bacterial PAMP mimic that activates TLR4) for 5 h after which cell supernatant was collected and the levels of the pro-inflammatory cytokine IL-6 were quantified. Higher levels of secreted IL-6 are indicative of a TLR tolerant phenotype [78]. This experimental setup allowed for the induction of TLR tolerance *ex vivo* by first exposing monocytes to a viral PAMP (Poly I:C) and then to a bacterial PAMP (LPS). This sequential stimulation also would recapitulate the inflammatory exposure seen by monocytes in ICU patients with COVID-19, due to their viral infection, followed by any secondary bacterial infection. Using this experimental design, we found that monocytes treated with either LPS or Poly I:C alone secreted lower levels of IL-6 when compared to monocytes sequentially treated with Poly I:C then LPS. In fact, sequentially treated monocytes produced at least 1.2-fold more IL-6 than monocytes treated with Poly I:C or LPS alone. However, the addition MnO nanoparticles was able to completely abrogate IL-6 production in monocytes sequentially treated with Poly I:C then LPS. Thus, treatment with the MnO DAMP/PAMP nanoscavenger can significantly reduce IL-6 production by monocytes in response to sequential TLR stimulation and thereby limit induction of a TLR tolerance phenotype (Fig. 9C).

4. Discussion

In this study, we performed immune and molecular assays that demonstrated elevated levels of nucleic acid-containing DAMPs/PAMPs are present in COVID-19 ICU patient serum and ETA. We also observed a monocytic TLR tolerance phenotype in deceased COVID-19 ICU patients. We established that two biomaterials could potentially be used to mitigate DAMP/PAMP-mediated hyperinflammation. TLR activation analyses using patient serum and ETA revealed systemic and local inflammation as indicated by potent stimulation of TLR3, TLR4, TLR7, and TLR9 signaling. DAMPs and PAMPs, which were particularly high in the airways, likely spill into the systemic circulation, resulting in hyperinflammation via persistent TLR stimulation. We observed that compared to deceased COVID-19 ICU patients those that recover have a higher abundance of $CD16^{+}$ monocytes, which are known to be responsive to TLR7/8 activation by viral ssRNA. We characterized the functional differences in these monocytes and found that patients with different clinical outcomes mount a differential response to prototypic viral and bacterial PAMPs [31]. To characterize the monocytes in ICU survivors and non-survivors, we measured the response of monocyte subsets following activation with TLR agonists and also assayed the serum proteome from patients. These immune profiling, transcriptomic and proteomic analyses all suggested that nucleic acid-containing DAMPs/PAMPs play a central pathological role in the critically ill COVID-19 ICU patients. We therefore explored whether nucleic acid-scavenging agents could be utilized to counteract such DAMPs/PAMPs in samples from these ICU patients. We describe two complementary biomaterial-based approaches, microfibers and soluble nanoparticles, to neutralize the activation potential of these hyperinflammatory lung and blood samples.

By stimulating isolated monocytes from deceased and recovered patients with TLR agonists, we discovered that cells with the same cytometric phenotype contain distinct molecular biomarkers and undergo differential transcriptional responses that distinguish between patients with different clinical outcomes. Overall, monocytes from recovered patients produce a robust anti-viral response to TLR activation, whereas monocytes from deceased patients amplify the effects of the cytokine storm observed in COVID-19 patients via expression of TNF-α and alarmin mRNAs. These molecular patterns observed in deceased patients are congruent with the concept of TLR tolerance, marked by the lack of IL-12 production induced by the MAPK and AP-1 signaling pathway [15,32–36]. Indeed, we identified transcriptomic profiles consistent with the previous characterization of IL-12 production in innate myeloid cells from mice in which TLR tolerance was induced with a primary viral infection and a secondary bacterial infection [79,80]. However, $CD16^{+}$ monocytes from deceased ICU patients with COVID-19 had reduced expression of JUND at baseline and did not activate the AP-1 signaling pathway upon stimulation with LPS or R848 (Fig. 5A, G-I). This observation suggests that tolerant monocytes lose the ability to produce IL-12 and leave the patients at increased risk of secondary bacterial infection [37,40,81]. Therefore, increased and prolonged inflammation during severe SARS-CoV-2 infection can engender

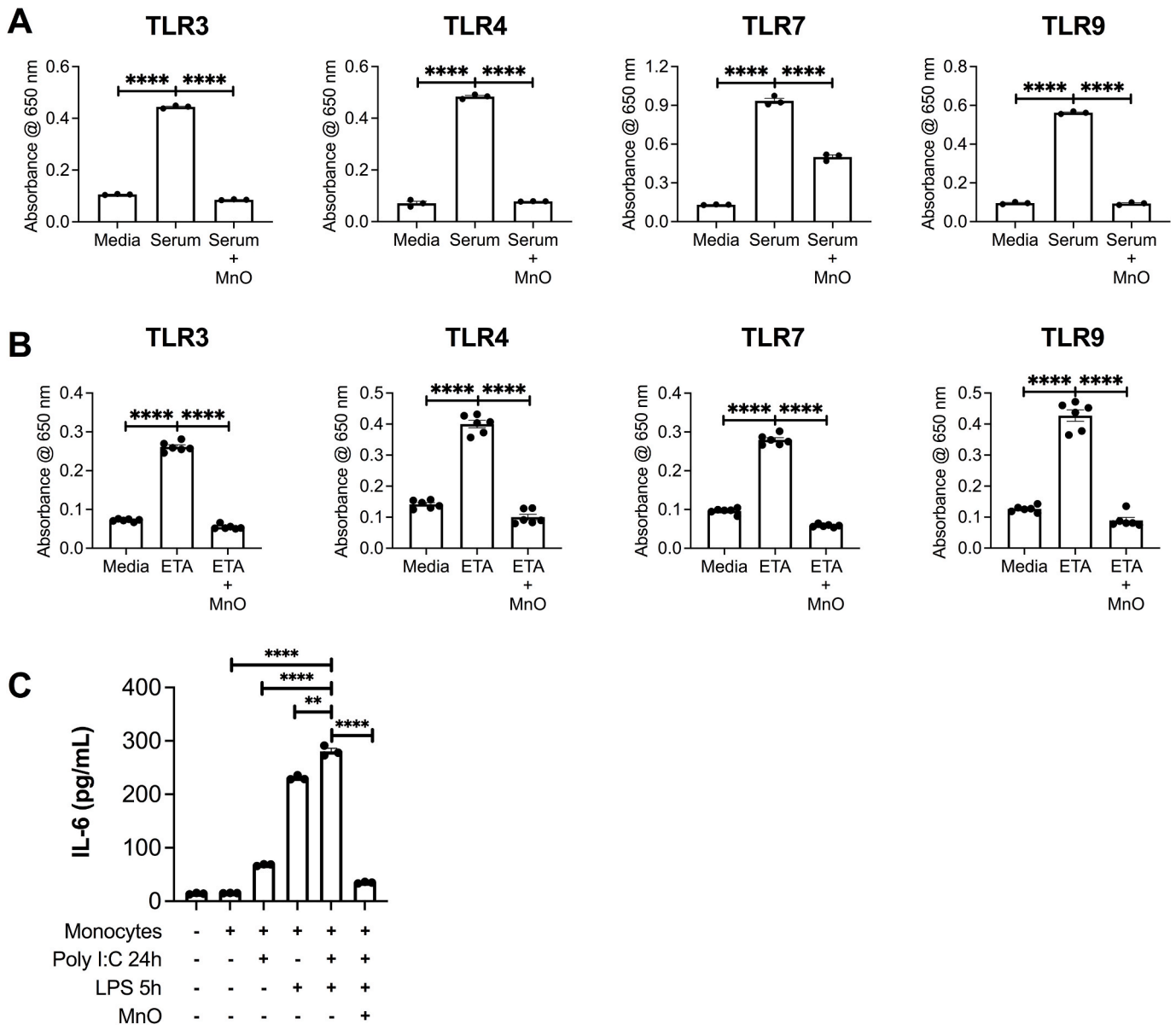

Fig. 9. Manganese Oxide (MnO) nanoparticles reduce the activity of TLR activating PAMPs/DAMPs in COVID endotracheal aspirate (ETA) and serum and prevent DAMP/PAMP-mediated TLR tolerance in monocytes. MnO significantly reduces stimulation of TLRs 3, 4, 7, and 9 by COVID-19 serum in TLR reporter cell assays. **B.** MnO significantly reduces stimulation of TLRs 3, 4, 7, and 9 by COVID-19 ETA in TLR reporter cell assays. **C.** Freshly isolated monocytes were treated with or without Poly I:C (double-stranded viral RNA DAMP mimic) for 24 h (24 h), followed by treatment with or without lipopolysaccharide (LPS, bacterial DAMP mimic) for 5 h (5 h) after which cell supernatant was collected and IL-6 levels were quantified. Treatment with MnO was able to significantly reduce IL-6 production by monocytes in response to sequential TLR stimulation. ** = $p < 0.01$ via 2-tailed *t*-test; **** = $p < 0.0001$ via 2-tailed *t*-test.

an immunosuppressed phenotype that prevents adequate response to subsequent infections which can lead to poor clinical outcomes. Our data show that deceased patients not only have TLR tolerant monocytes, but that a second independent group of deceased patients has significantly elevated proteinaceous markers of severe bacterial infection. Our proteomics data reveal that patients who eventually died in the ICU had significantly lower levels of PAMP and DAMP carrier proteins in their blood such as MARCO and apolipoproteins, including APOA1, APOA2, APOH, and APOD, especially at later time points of infection. MARCO and apolipoproteins have been shown to protect against bacterial infection due to their ability to bind to PAMPs and transport them to immune cells as well as neutralize LPS to temper cytokine storms [73–77]. A decrease in the circulating levels of these factors most likely results from the consumption of PAMP carriers due to the prolonged abundance of their ligands, which is consistent with TLR hyper-activation and also likely predisposes these patients to secondary bacterial infection.

Unfortunately, previous studies have shown that it is difficult to rescue monocytes that have become TLR tolerant [37]. Therefore, a therapeutic strategy designed to treat or stop COVID-19 patients from becoming critically ill will almost assuredly need to prevent the development of TLR tolerance in the first place. With this in mind, we evaluated a strategy to neutralize TLR agonists using nucleic acid-binding microfibers and nanoparticles, effectively supplementing the function of the depleted endogenous PAMP scavengers MARCO and apolipoprotein. As we and others have shown in models of trauma, sepsis, cancer, influenza and now COVID-19, neutralizing or removing DAMPs and PAMPs from circulation using nucleic acid binding biomaterials can reduce systemic inflammation and TLR tolerance by preventing TLR activation [11–17,21,22]. The microfiber mesh strategy can

theoretically be modified for use in a variety of devices, including filters for dialysis and extracorporeal membrane oxygenation (ECMO) that are commonly used to treat ICU patients with COVID-19 [82]. MnO-based nanoscavengers can be used for systemic or inhalation delivery in patients before the need for invasive airway support. Patients that are intubated due to virally induced respiratory failure are predisposed to a secondary ventilator-associated bacterial pneumonia (VAP) [83–85]. These bacteria are recognized by their surface expression of the virulence factor LPS. A secondary immune challenge with LPS in mice caused a severe inflammatory reaction and high mortality, defining a similar trajectory to those observed in ICU patients who die from COVID-19 [81,86]. TLR tolerance leads to the inability of monocytes to adequately respond to subsequent immune challenges, as in the case of VAP associated with COVID-19 and poor outcomes. MnO might prove useful to supplement and replenish endogenous scavengers that are being overrun by PAMPs/DAMPs in the critically ill with COVID-19. As shown in Fig. 9, MnO nanoscavengers limit TLR stimulation by COVID-19 patient samples. By limiting TLR stimulation, such nanoparticles should abrogate TLR tolerance of patient monocytes caused by TLR hyperstimulation.

The *in vivo* translation of this DAMP/PAMP neutralization concept now needs to be tested to determine it can improve outcomes in the setting of COVID-19 infection as has been observed in other animal models of disease [11–14,16,17]. Of particular relevance to SARS-CoV-2 infection, we have shown that neutralization of DAMPs/PAMPs improves outcomes in animal models of influenza and sepsis [13,19,20]. Future studies using a large animal model of COVID-19 that recapitulates the TLR tolerance phenotype observed in COVID-19 ICU patients should be pursued to allow for the establishment of an ECMO animal model in which the utility of the proposed microfiber-based DAMP/PAMP capture strategy could be characterized. We did not examine whether similar TLR-tolerant monocytes are associated with patients with non-COVID-19 ARDS but hypothesize that a common immunopathology may underlie dysfunction in sepsis and other severe infections, as well. Furthermore, we were unable to investigate the role of neutrophils and platelets, which also express TLRs and have been implicated in COVID-19 thromboinflammatory syndromes. Future studies using fresh blood are needed to compare the contributions of these cells to the TLR-mediated inflammatory response in COVID-19 and other infectious diseases and the potential utility of microfiber and nanoparticle-based DAMP/PAMP scavengers to control such hyperinflammation.

In summary, we observe that nucleic acid-containing DAMPs/PAMPs are highly elevated in the lungs and blood of COVID-19 ICU patients and that $CD16^+$ monocytes isolated from such patients are defined by TLR activation phenotypes that reflect the clinical outcome. Specifically, patients that recover from SARS-CoV-2 infection have $CD16^+$ monocytes capable of producing a competent anti-viral immune response through activation of TLRs such as TLR7/8, while cells from deceased patients are tolerized to TLR activation due to chronic, repeated DAMP/PAMP-induced inflammation. We observed that monocytes from deceased patients have transcriptomic and proteinaceous markers characteristic of TLR tolerance consistent with the observation that nucleic acid DAMPs/PAMPs are highly elevated in patient serum and ETA. We tested two complementary approaches to neutralize such inflammatory mediators that if developed appropriately might prevent hyperinflammation, monocytic TLR tolerance and improve clinical outcomes for individuals who are severely ill with COVID-19.

5. Materials and methods

5.1. COVID-19 ICU study population

The study was approved by the Duke University Institutional Review Board (IRB) (Pro 00101196). Eligible patients were men and women ages 18 years and above that were admitted to an adult ICU at Duke University Hospital with SARS-CoV-2 infection confirmed by PCR testing. Informed consent was obtained from the patient or their Legally Authorized Representative (LAR).

5.2. Duke ICU COVID-19 biorepository

We collected whole blood and endotracheal aspirate (ETA) supernatants. Whole blood was separated into serum, citrated plasma, EDTA (ethylenediaminetetraacetic acid) plasma, and peripheral blood mononuclear cells (PBMCs). ETA was spun down at 600 g for 10 min at 4 °C. The supernatant was pipetted off and the pellet and supernatant were stored at −80 °C. Samples were collected on study days 1, 3, 7, 14, and 21. All data reported in this paper were obtained with patient samples from the Duke ICU Biorepository and this study was performed in collaboration with the Biorepository team.

5.3. Healthy controls

Whole blood was collected from healthy donors under a separate protocol approved by the Duke IRB (Pro 00007265) and processed similarly.

5.3.1. Reagents

Pooled human serum from healthy donors was purchased from Sigma Aldrich. CpG ODN 2006, Poly I:C, LPS, and R848 were purchased from InvivoGen. ELISA kits were purchased as follows: HMGB-1 (Tecan-ST51011), Cell-Death Detection ELISA Plus (Roche-11,774,425,001), and albumin (Abcam-ab179887). Picogreen and Ribogreen stains were obtained from Life Technologies (P7589 and R41190). PAMAM-G3 based nucleic acid binding fiber and polyethylenimine (PEI)-based nucleic acid binding fiber were graciously provided by Jaewoo Lee, PhD and synthesized as previously described [15].

5.3.2. Synthesis of nucleic acid binding Fiber and removal of TLR Ligands from Serum and ETA

Electrospinning was utilized to generate nucleic acid-binding microfibers as previously described [15]. Briefly, poly (styrene-*alt*-maleic anhydride) (PSMA) polymers meshes were used to functionally immobilize [87,88] PAMAM-G3 or PEI onto microfiber meshes containing a mixture of PSMA and polystyrene copolymers. PSMA (0.3 g) (Sigma, Saint Louis, MO) and polystyrene (0.4 g) (Sigma) were dissolved at room temperature in a 1:1:1 (v:v:v) mixture of tetrahydrofuran:acetone:dimethylformamide (3 mL) (Sigma) and microfibers were generated by electrospinning 2 mL of copolymer solution at a dispensing rate of 2 mL/h with an applied voltage of ~17.3 kV, as described previously [87,89]. To generate microfiber meshes, the microfibers were collected on a grounded cylindrical mandrel as described [15]. To immobilize PEI and PAMAM-G3 on the PSMA/polystyrene microfiber meshes 1.8 kDa branched polyethylenimine (PEI) (Polysciences, Warrington, PA) (0.005 M) and PAMAM-G3 (0.004 M) (Sigma) were incubated for 72 h either at room temperature (PEI) or 4 °C (PAMAM-G3) as described [15].

Patient sera [10 μL] or ETA [1 μL] were diluted into a final volume of 100 μL with serum-free AIM-V media. Dilutions were incubated with PAMAM-G3-based fiber at 37 °C for 30 min with rotation. The suspension was removed and combined with a PEI-based fiber and a PAMAM-based fiber for 30 min each at 37 °C with rotation prior to use in TLR reporter assays. This sequential fiber-based strategy was validated as the most effective scavenging fiber approach in previous studies [15].

5.3.3. MnO nanoparticle Synthesis and neutralization of TLR Ligands from Serum and ETA using MnO nanoparticles

Manganese oxide can be synthesized by using manganese compounds (e.g., manganese acetate) and acid (e.g., tannic acid) at high temperature (e.g., 100–150 °C). A mixture of manganese acetate and tannic acid (mass ratio of manganese acetate and tannic acid is 1 : 2–6)

in Milli-Q water is stirred for 10 min at room temperature, the solution is then transferred into an autoclave. After heat treatment at 150 °C for 2 h, the sample solution is cooled to <50 °C naturally. The size of MnO nanoparticles ranged from 30 to 100 nm and zeta potential is about −20 mV.

Patient sera [10 μL] or ETA [1 μL] were diluted into a final volume of 100 μL with serum-free AIM-V media. Dilutions were incubated with MnO at 37 °C for 30 min with rotation prior to use in TLR reporter assays and monocyte stimulation assays.

5.4. Whole blood flow cytometry

Immune subset profiling antibody panels were obtained from Beckman-Coulter. One basic immune subset panel tube (B53309) and one granulocyte panel tube (B88651) was used per patient, per time point per the manufacturer's instructions. The fixed and stained cells were acquired within two days of collection by The Duke Immune Profiling Core (DIPC) in accordance with BSL2* biosafety practices. Data were analyzed using FlowJo.

5.5. TLR activation assays

HEK-Blue human TLR 3, 4, 7, and 9 reporter cell lines were purchased from Invivogen (hkb-htlr3, hkb-htlr4, hkb-htlr7, hkb-tlr9). Activation was determined according to the manufacturer's instructions using QUANTI-blue SEAP detection media (InvivoGen). Cells were plated in 96-well plates at a density of 40,000 cells/well and treated for 12 h with media, LMW PolyI:C [1 μg/mL], LPS [1 μg/mL], R848 [1 μg/mL], or CpG ODN 2006 [1 μM], pooled healthy human sera [10 μL], COVID-19 patient sera [10 μL], or COVID-19 patient ETA [2 μL] in a final volume of 100 μL media. Cell supernatant was collected and mixed with QUANTI-blue at a 20:80 vol:vol ratio and incubated for 90 min at 37 °C. Absorbance was measured using a Spectramax i3 plate reader (Molecular Devices) at 655 nm. All samples were run in triplicate and results are reported as comparative absorbance values.

5.5.1. Single Cell RNA sequencing of monocytes from COVID-19 ICU patients

PBMC's that were isolated and frozen as part of the ICU Biorepository (see above) were used for this experiment. PBMC's from 3 patients that recovered and 3 patients that died earlier in the pandemic, who did not receive the anti-inflammatory/immunomodulatory drug dexamethasone was used. PBMCs were thawed at 37 °C and resuspended in AIM-V media lacking FBS. Thereafter, monocytes were isolated from total PBMCs using Stem Cell's bead-based isolation kit (19,058). Isolated monocytes from each patient were then distributed into 3 wells of a low-binding 24-well plate (Corning-3473). These monocytes were then treated with media, LPS (1 μg/mL), or R848 (1 μg/mL) for 6 h at 37 °C. These monocytes were then washed once with warmed AIM-V media and taken to our single-cell RNA sequencing core.

Cells were stained with TotalSeq-B anti-human Hashtag antibodies (Biolegend – San Diego, CA #394631, 394,633, 394,635, 394,637, and 394,639) following the manufacturer's protocol, with minor modifications. Cells were counted on a Cellometer (Nexcelom - Lawrence, MA) using propidium iodide and acridine orange to ensure accuracy of count and viability. Cells were resuspended in 50 μL cell stain buffer (CSB, Biolegend– San Diego, CA #420201) with 5 μL Human TruStain™ Fc Blocking Reagent (Biolegend– San Diego, CA #422301) and incubated on ice for 10 min. Following Fc block, the incubation supernatant was removed and each cell sample was stained with previously determined hashtag antibody according to the table below and incubated on ice for 30 min.

After incubation cells were washed 3 times, resuspended at a concentration of 1.5×10^6 cells/mL, and filtered with a 40 μm Flowmi Cell Strainer (Bel-Art H13680-0040). Hashtag-stained cells were pooled according to table (2000 cells per sample, 4 or 5 samples per pool) and loaded onto 10x Genomics NextGEM chip.

Four gene expression and four hashtag oligo libraries were generated with the Chromium Next GEM Single Cell 3′ v3.1 assay (10x Genomics PN-1000128), Chromium Next GEM Chip G Single Cell Kit (PN-1000127), and Single Index Kit Set A (PN-1000127), following the Chromium Next GEM Single Cell 3' Reagent Kits v3.1 with feature barcoding technology for cell surface protein protocol CG000206 version D. Cells were resuspended in a master mix that contains reverse transcription (RT) reagents and then combined with gel beads carrying the Illumina TruSeq Read 1 sequencing primer, 16 nt 10x barcode, 12 nt unique molecular identifier and a poly-dT primer for RT. Full-length cDNAs were purified with Dynabeads MyOne SILANE, followed by cDNA amplification for 11 cycles. Amplified cDNA was assayed on a 4200 TapeStation High Sensitivity D5000 ScreenTape (Agilent - Santa Clara, CA) to ensure lengths between 200 and 5000 bp. Enzymatic fragmentation and size selection were used to optimize the cDNA amplicon size before Illumina (San Diego, CA) P5 and P7 adapters, i5 sample indexes, and TruSeq read 2 primers were added via End Repair, A-tailing, Adaptor Ligation, and PCR. KAPA Library Quant qPCR (Roche KK4873) was used to assess P5 and P7 adapter ligation on an ABI ViiA 7 (Applied Biosystems, Foster City, CA), prior to assay on an Agilent 4200 TapeStation with the High Sensitivity D1000 ScreenTape to size the libraries between 400 and 500bp. The sequence was generated using paired-end sequencing on an Illumina NovaSeq 6000 on a paired-end, single indexed flow cell at ~50,000 reads/cell.

Sample Name	Hashtag Antibody #	Cell Pool
C4 Media	1	1
C5 Media	2	1
C4 LPS	4	1
C5 LPS	5	1
C7 LPS	1	2
C4 R848	2	2
C5 R848	3	2
C7 R848	4	2
H11 Media	1	3
H18 Media	2	3
H24 Media	3	3
C7 Media	4	3
H11 LPS	5	3
H18 LPS	1	4
H24 LPS	2	4
H11 R848	3	4
H18R848	4	4
H24 R848	5	4

5.5.2. scRNA-seq dataset processing and cell type annotation

Following sequencing, datasets were demultiplexed using the 10x Genomics Cell Ranger pipeline to generate FASTQ files and feature count matrices. The hashtag-labeled reads were mapped to the respective sample using the HTODemux () function implemented by Seurat 3 and all default parameter values [90]. Cells with fewer than 200 or greater than 3500 genes detected were removed from downstream analysis. Similarly, cells with greater than 10% of reads mapping to the mitochondrial genome were removed from the datasets. Gene counts were log-normalized and the top 2000 variable features were identified for dataset integration. The datasets were merged into a single Seurat object using the FindIntegrationAnchors () and IntegrateData () functions with the number of dimensions set to 30. Principal component analysis and UMAP dimensionality reduction were performed using the first 30 principal components. The Seurat function SCTransform () was applied to the integrated dataset, and UMAP embeddings were recalculated using the Harmony package, taking into account the first 20 principal components [91]. Graph-based clustering was then performed with resolution = 1. Cell type annotation was performed using the

single-cell RNA-seq references provided with the SingleR package [92]. Specifically, cells were labeled as $CD16^-$monocytes or $CD16^+$ monocytes based on annotation with the DatabaseImmuneCellExpressionData () function. Cells that were not annotated as monocytes were removed from downstream analysis. Cell type labels were confirmed by plotting the expression density of CD14 and FCGR3A (CD16) for all cells as a UMAP with the Nebulosa package [93].

5.5.3. Univariate Testing for differential expression in scRNA-seq datasets

Pseudo-bulk univariate testing was performed for all samples using aggregate single-cell gene expression profiles for either $CD16^-$monocytes or $CD16^+$ monocytes. Cells from recovered patients were compared to cells from deceased patients in each of three conditions: media, LPS, or R848. MDS ordination plots were generated using the EdgeR package to performed dimensionality reduction for each monocyte sub-population [94,95]. Polygons were plotted over the MDS embeddings to visualize clusters of samples. Gene expression profiles for each cell type were aggregated into a single matrix to perform univariate testing using the EdgeR pipeline. The design formula for univariate testing incorporated subject outcomes, and differential gene expression testing was performed for both $CD16^-$monocytes and $CD16^+$ monocytes under each of the three conditions. Log-fold change enrichment and FDR-corrected p-values were plotted using the EnhancedVolcano package (https://github.com/kevinblighe/EnhancedVolcano). Significance was defined as absolute log-fold change >0.5 and FDR-corrected p-value < 0.05. Intersections in the differentially expressed gene sets were calculated and visualized as UpSet plots [96]. Functional enrichment analysis was performed for the genes with higher expression in $CD16^+$ monocytes from deceased patients using g:Profiler and pathway-level enrichment is reported as FDR-corrected p-values [97].

5.5.4. Non-negative matrix factorization applied to monocyte subsets

The CoGAPS implementation of non-negative matrix factorization was applied to media, LPS, and R848-treated monocytes separately [98]. Genes with high technical variance, including mitochondrial and ribosomal protein genes, were removed from the analysis. Five gene expression patterns were identified for each cell population using 500 iterations. The CoGAPS loadings for each experiment were used to identify the top 10 genes associated with each of the five patterns. These genes were visualized as a heatmap to give context for genes with correlated expressions that make up each pattern. The CoGAPS scores assigned to each cell were plotted as violin plots to identify multi-modal distributions of cells that have a similar expression to the five gene expression patterns. Distributions in pattern scores that stratified monocyte sub-populations by clinical outcome were plotted as scatter plots and used to define univariate testing comparisons. Functional enrichment analysis was performed for these differentially expressed genes to estimate pathways enrichment associated with clinical outcome.

5.6. Gene regulatory network inference

The scRNA-seq Seurat object was converted into a SingleCellExperiment and used as input to analysis with the SCENIC package [99]. Genes with differential expression between $CD16^+$ monocytes from recovered and deceased subjects were identified for each treatment condition. The standard workflow for running the SCENIC analysis was then performed using the count matrix for these marker genes as input [100]. GENIE3 was used to identify regulons including transcription factors and regulatory targets with correlated co-expression, and AUCell was used to score regulon activity for each monocyte sub-population. The 'top10perTarget' co-expression parameter was used to prune the list of scored regulons. Regulon activity z-scores were plotted as a heatmap to identify enrichment associated with clinical outcome.

Genes regulated by the transcription factor NFκB were retrieved from the KEGG functional annotation database and used to visualize trends in expression associated with clinical outcome [101]. The average expression of each pathway gene was calculated using Seurat, and the mean expression was calculated using all of the pathways genes together. Expression of NFKBIA was plotted against expression of JUND as a scatter plot, and the correlation was calculated using all $CD16^+$ monocytes.

5.6.1. Plasma proteomics with COVID-19 ICU patient specimens

This experiment was conducted by the Duke Proteomics Core. Samples were thawed, and 20 μL of plasma was aliquoted into 750 μL Matrix tubes (Thermo) in a 96-well format. A study pool QC (SPQC) sample was made by mixing equal volumes of all samples. Three replicates of the SPQC sample were added to the plate. Samples were diluted with 200 of 5.5% w/v sodium deoxycholate (SDC) in 50 mM ammonium bicarbonate (AmBic) containing 11 mM dithiothreitol, and samples were inactivated by heating at 80 °C for 15 min. After cooling, samples were alkylated with 10 μL of 250 mM iodoacetamide (IAM) in AmBic at room temperature in the dark, for 30 min. Alkylation was quenched by addition of 10 μL of 220 mM DTT in AmBic, and digestions were performed by adding 20 μL of 5 mg/mL TPCK trypsin (Sigma) in AmBic followed by incubation at 37 °C for 2 h in a Thermomixer. Reactions were quenched by addition of 30 μL of 5/20/65 v/v/v TFA/MeCN/water containing 0.33 pmol yeast ADH1 digest (Waters MassPrep) to each sample followed by brief vortexing and incubation on a Thermocycler for 5 min and centrifugation for 2 min at 10,000×*g*. 15,000×*g* for 2 min, supernatants and residual precipitate were transferred to an ISOLUTE Filtration + filter plate (Biotage) taped to a Deepwell 96/1000 μl plate (Eppendorf) followed by shaking at 1250 rpm for 3 min. Finally, the samples were filtered for 10 min on a vacuum manifold in a 96-well plate and sealed with a cap mat.

Quantitative data-independent acquisition (DIA)-LC-MS/MS. Samples were analyzed by DIA-LCMS/MS using an Acquity UPLC (Waters) interfaced to a Exploris 480 high-resolution tandem mass spectrometer (Thermo). Analyses of plasma samples used 10 μL of peptide digests (~33 μg). After direct injection, peptides were separated on a 1 mm × 15 mm 1.7 μm CSH C18 column (Waters) using a flow rate of 100 μL/min, a column temperature of 55 °C and a gradient using 0.1% (v/v) formic acid (FA) in H2O (mobile phase A) and 0.1% (v/v) FA in MeCN (mobile phase B) as follows: 0–60 min, 3–28% B; 60–60.5 min, 28–90% B; 60.5–62.5 min, 90% B; 62.5–63 min, 90-3% B; and 63–67 min, re-equilibration at 3% B. A tee was used post-column to introduce a solution of 50% (v/v) dimethyl sulfoxide/acetonitrile (DMSO/MeCN) at 10 μL per min. The LC was interfaced to the MS with an Optamax NG ion source under heated electrospray ionization (HESI) conditions with the following tune parameters: sheath gas, 32; aux gas, 5; spray voltage, 3.5 kV; capillary temperature, 275 °C; aux gas heater temp, 125 °C.

The DIA analysis used a 120,000 resolution precursor ion (MS1) scan from 375 to 1600 *m/z*, AGC target of 300% and maximum injection time (IT) of 45 miliseconds and RF lens of 40%; data were collected in centroid mode. MS/MS was performed using tMS2 method with default charge state = 3, 30,000 resolution, AGC target of 1000% and maximum IT of 60 ms, and a NCE of 30; data were collected in centroid mode. 18 variable DIA windows spanned 400–1200 *m/z*. The MS cycle time was 1.65 s, and the total injection-to-injection time was 67 min.

High pH-reversed phase (HPRP) fractionation for Spectral Library Generation. Approximately 500 μg of protein digests, pooled from individual samples, was lyophilized and resuspended in 20 mM ammonium formate, pH 10. Peptides were fractionated using a 2.1 mm × 5 cm BEH C18 column (Waters) and Waters ACQUITY I-Class UPLC. Separations utilized a flow rate of 0.4 mL/min and column temperature of 55 °C, and mobile phases consisted of 20 mM ammonium formate, pH 10 (MPA) and neat MeCN (MPB). A gradient was as follows: 0–3, 3% MPB; 3–50 min, 3–35% MPB; 50–51 min, 35–90% MPB; 51–55 min, 90% MPB; 55–56 min, 90-3% MPB; 56–70 min, 3% MPB. 48 equal fractions were collected from 3 to 53 min (~0.4 mL each fraction) into wells

containing 10 μl of 40% TFA, and each column of wells (e.g. wells/fractions 1, 13, and 25 and 37) was combined to maximize the peak capacity of the LCMS/MS analyses. After lyophilization, samples were resuspended in 25 μl of 1% (v/v) TFA/2% (v/v) MeCN in H_2O.

Qualitative analysis of HPRP-fractionated samples for Spectral Library Generation. Twenty μL of each of the fractionated pools (12 fractions each) were analyzed by microflow LC-MS/MS as described above, except that the data was analyzed in Spectronaut 14 using the study-specific library. To minimize missing data, "profiling" was used to quantify precursors that did not meet a significance value (q-value <0.01) in every run. Using a sparse cut-off of 20% (data included all precursors that met a q-value in at least 20% runs), there were 559 proteins quantified in the plasma samples. Of these, 450 proteins (including ADH1, trypsin, and 3 variant protein entries) were quantified by more than 1 unique precursor, a metric for more confident identification.

Normalization: Raw protein group data (sum of all quantified precursors) was normalized by Library Size, followed by Trimmed Mean of M (TMM) normalization. Normalization had little effect on expression measurements, suggesting highly stable sample preparation, data acquisition and overall protein content between the study samples measured.

Data analysis: Normalized data was first evaluated grouping all patient timepoints by outcome, to narrow down the dataset we performed multiple T tests with Benjamini-Hochberg (BH) correction and proceeded with proteins meeting the threshold of adjusted $p < 0.05$. Using the average protein measurements by outcome we calculated the log 2 fold changes for each protein, and grouped upregulated and downregulated proteins separately. These were analyzed in STRING V 11.0 for full STRING network at a required score of highest confidence (0.900) ignoring disconnected nodes, and g:Profiler (version e103_eg50_p15_68c0e33) using default settings [97,102]. We then proceeded with pathway clustering using Enrichmentmap 3.3 application via Cytoscape 3.8, using downloaded pathway and enrichment data from g:Profiler [103,104]. We narrowed on hits consistent with the most enriched pathway clusters, namely defense/immune cell pathways for upregulated proteins, and wound healing/complement and immunity for downregulated genes.

We further evaluated the hits differences between outcome by matched timepoints at 0, 7 or 14-days using T tests to find out when these proteins were most likely to have differences.

5.6.2. ELISA and nucleic acid quantification

ELISA, Picogreen, and Ribogreen assays (Life Sciences) were performed per the manufacturer's instructions in triplicate.

5.6.3. Statistical analysis

Statistical tests were performed in GraphPad Prism via one-way ANOVA followed by Sidak multiple comparison test between healthy sera controls and COVID-19 samples or between COVID-19 sample types. All other graphs were created with GraphPad Prism software.

Funding

This study was funded by:
Discretionary funds from Duke Department of Surgery.
Development of methods used in the project was funded by:
Department of Defense Breast Cancer Research Program award W81XWH-16-1-0354 (SKN), W81XWH-19-1-0463 (KWL) and National Institutes of Health (NIH) grant R01AR073935 (BAS and KWL).

Author contributions

Conception: SKN, BAS, NG, IAN; Study Design: SKN, IAN, NG, TL, LO, BAS; Clinical samples: LQ, BK, LC; Study implementation: TL, LO, SAM, IAN; Single cell RNA-seq: NG, KB, SA, XS; Data analysis and interpretation: SKN, IAN, NG, TL, LO, SAM; Figures and visualization: NG, TL, IAN, SB, Project administration: SKN, BAS; Writing—original draft: IAN, NG, TL, Writing—review & editing: IAN, NG, TL, LO, SAM, SB, SA, KA, LC, LQ, BK, XS, JL, KWL, SKN, BAS; Materials Synthesis: TOA, YuZ, YiZ, JL. Classification: Major-Biological Sciences | Minor-Immunology and Inflammation.

Data and materials availability

All data are available in the main text or supplementary materials.

Declaration of competing interest

The authors declare the following financial interests/personal relationships which may be considered as potential competing interests: Smita Nair, Kam Leong and Ibtehaj Naqvi have a patent pending.

Acknowledgments

We are extremely grateful to David Montefiori, PhD for helpful discussions, resources and infrastructure support and Guido Ferrari, MD for helpful discussions and advice. We would like to acknowledge David Boczkowski for his help in flow cytometry and PBMC isolation and stimulation. We would also like to acknowledge John Yi and the Duke Immune Profiling Core, Department of Surgery, without whom our immune profiling would have been impossible. We would also like to acknowledge Matthew Foster and the Duke Proteomics Core for their help in processing the plasma samples and aiding our team in acquiring the data. We thank Simon Gregory, PhD for discussions related to single-cell RNAseq. This work used a high-performance computing facility partially supported by grants 2016-IDG-1013 and 2020-IIG-2109 from the North Carolina Biotechnology Center.

Appendix A. Supplementary data

Supplementary data to this article can be found online at https://doi.org/10.1016/j.biomaterials.2022.121393.

References

[1] R. Medzhitov, Origin and physiological roles of inflammation, Nature 454 (7203) (2008) 428–435.
[2] G.M. Barton, A calculated response: control of inflammation by the innate immune system, J. Clin. Invest. 118 (2) (2008) 413.
[3] J.D. Hansen, L.N. Vojtech, K.J. Laing, Sensing Disease and Danger: a Survey of Vertebrate PRRs and Their Origins, Developmental & Comparative, 2011.
[4] S. Rakoff-Nahoum, R. Medzhitov, Toll-like receptors and cancer, Nat. Rev. Cancer 9 (1) (2009) 57–63.
[5] K. Bhatelia, K. Singh, R. Singh, TLRs: linking inflammation and breast cancer, Cell. Signal. 26 (11) (2014) 2350–2357.
[6] S. Pandey, S. Singh, V. Anang, A.N. Bhatt, K. Natarajan, B.S. Dwarakanath, Pattern recognition receptors in cancer progression and metastasis, Cancer Growth Metastasis 8 (2015) 25–34.
[7] M. Mehmeti, R. Allaoui, C. Bergenfelz, L.H. Saal, S.P. Ethier, M.E. Johansson, K. Jirstrom, K. Leandersson, Expression of functional toll like receptor 4 in estrogen receptor/progesterone receptor-negative breast cancer, Breast Cancer Res. 17 (1) (2015) 130.
[8] S. Gonzalez-Reyes, L. Marin, L. Gonzalez, L.O. Gonzalez, J.M. del Casar, M. L. Lamelas, J.M. Gonzalez-Quintana, F.J. Vizoso, Study of TLR3, TLR4 and TLR9 in breast carcinomas and their association with metastasis, BMC Cancer 10 (2010) 665.
[9] S. Sun, T. Sursal, Y. Adibnia, C. Zhao, Y. Zheng, H. Li, L.E. Otterbein, C.J. Hauser, K. Itagaki, Mitochondrial DAMPs increase endothelial permeability through neutrophil dependent and independent pathways, PLoS One 8 (3) (2013), e59989.
[10] Z. Feng, S. Qi, Y. Zhang, Z. Qi, L. Yan, J. Zhou, F. He, Q. Li, Y. Yang, Q. Chen, S. Xiao, Q. Li, Y. Chen, Y. Zhang, Ly6G+ neutrophil-derived miR-223 inhibits the NLRP3 inflammasome in mitochondrial DAMP-induced acute lung injury, Cell Death Dis. 8 (11) (2017) e3170-e3170.
[11] E.K. Holl, K.L. Shumansky, L.B. Borst, A.D. Burnette, C.J. Sample, E.A. Ramsburg, B.A. Sullenger, Scavenging nucleic acid debris to combat autoimmunity and infectious disease, Proc. Natl. Acad. Sci. U. S. A. 113 (35) (2016) 9728–9733.
[12] E.K. Holl, J.E. Bond, M.A. Selim, T. Ehanire, B. Sullenger, H. Levinson, The nucleic acid scavenger polyamidoamine third-generation dendrimer inhibits

fibroblast activation and granulation tissue contraction, Plast. Reconstr. Surg. 134 (3) (2014) 420–433.
[13] E.K. Holl, K.L. Shumansky, G. Pitoc, E. Ramsburg, B.A. Sullenger, Nucleic acid scavenging polymers inhibit extracellular DNA-mediated innate immune activation without inhibiting anti-viral responses, PLoS One 8 (7) (2013).
[14] I. Naqvi, R. Gunaratne, J.E. McDade, A. Moreno, R. Rempel, D.C. Rouse, S. G. Herrera, D.S. Pisetsky, J. Lee, R.R. White, B.A. Sullenger, Polymer-mediated inhibition of pro-invasive nucleic acid DAMPs and microvesicles limits pancreatic cancer metastasis, Mol. Ther. 26 (4) (2018) 1020–1031.
[15] J. Eppensteiner, J. Kwun, U. Scheuermann, A. Barbas, A.T. Limkakeng, M. Kuchibhatla, E.A. Elster, A.D. Kirk, J. Lee, Damage- and pathogen-associated molecular patterns play differential roles in late mortality after critical illness, Jci Insight 4 (16) (2019), e127925.
[16] S. Jain, G.A. Pitoc, E.K. Holl, Y. Zhang, L. Borst, K.W. Leong, J. Lee, B. A. Sullenger, Nucleic acid scavengers inhibit thrombosis without increasing bleeding, Proc. Natl. Acad. Sci. Unit. States Am. 109 (32) (2012).
[17] J. Lee, J.W. Sohn, Y. Zhang, K.W. Leong, D. Pisetsky, B.A. Sullenger, Nucleic acid-binding polymers as anti-inflammatory agents, Proc. Nat. Acad. Sci. 108 (34) (2011) 14055–14060. PMID: 21844380.
[18] H. Liang, B. Peng, C. Dong, L. Liu, J. Mao, S. Wei, X. Wang, H. Xu, J. Shen, H.-Q. Mao, X. Gao, K.W. Leong, Y. Chen, Cationic nanoparticle as an inhibitor of cell-free DNA-induced inflammation, Nat. Commun. 9 (1) (2018) 4291.
[19] J. Dawulieti, M. Sun, Y. Zhao, D. Shao, H. Yan, Y.-H. Lao, H. Hu, L. Cui, X. Lv, F. Liu, C.-W. Chi, Y. Zhang, M. Li, M. Zhang, H. Tian, X. Chen, K.W. Leong, L. Chen, Treatment of severe sepsis with nanoparticulate cell-free DNA scavengers, Sci. Adv. 6 (22) (2020), eaay7148.
[20] L. Kelly, L.B. Olson, R.E. Rempel, J.I. Everitt, D. Levine, S.K. Nair, M.E. Davis, B. A. Sullenger, β-Cyclodextrin-containing polymer treatment of cutaneous lupus and influenza improves outcomes, Mol. Ther. 30 (2021) 845–854.
[21] E.K. Holl, V. Frazier, K. Landa, D. Boczkowski, B. Sullenger, S.K. Nair, Controlling cancer-induced inflammation with a nucleic acid scavenger prevents lung metastasis in murine models of breast cancer, Mol. Ther. 29 (5) (2021) 1772–1781.
[22] E.O.U. Eteshola, K. Landa, R.E. Rempel, I.A. Naqvi, E.S. Hwang, S.K. Nair, B. A. Sullenger, Breast cancer-derived DAMPs enhance cell invasion and metastasis, while nucleic acid scavengers mitigate these effects, Mol. Ther. Nucleic Acids 26 (2021) 1–10.
[23] F. Zhou, T. Yu, R. Du, G. Fan, Y. Liu, Z. Liu, J. Xiang, Y. Wang, B. Song, X. Gu, L. Guan, Y. Wei, H. Li, X. Wu, J. Xu, S. Tu, Y. Zhang, H. Chen, B. Cao, Clinical course and risk factors for mortality of adult inpatients with COVID-19 in Wuhan, China: a retrospective cohort study, Lancet 395 (2020) 1054–1062.
[24] A.J. Rodriguez-Morales, J.A. Cardona-Ospina, E. Gutiérrez-Ocampo, R. Villamizar-Peña, Y. Holguin-Rivera, J.P. Escalera-Antezana, L.E. Alvarado-Arnez, D.K. Bonilla-Aldana, C. Franco-Paredes, A.F. Henao-Martinez, A. Paniz-Mondolfi, G.J. Lagos-Grisales, E. Ramírez-Vallejo, J.A. Suárez, L.I. Zambrano, W. E. Villamil-Gómez, G.J. Balbin-Ramon, A.A. Rabaan, H. Harapan, K. Dhama, H. Nishiura, H. Kataoka, T. Ahmad, R. Sah, L.A.N.o.C.D. Covid-Research, Clinical, Laboratory and Imaging Features of COVID-19: A Systematic Review and Meta-Analysis, Travel Med Infect Di, 2020, p. 101623.
[25] K.J. Goh, M.C. Choong, E.H. Cheong, S. Kalimuddin, S.D. Wen, G.C. Phua, K. S. Chan, S.H. Mohideen, Rapid progression to acute respiratory distress syndrome: review of current understanding of critical illness from COVID-19 infection, Ann. Acad. Med. Singapore 49 (1) (2020) 1–9.
[26] L. Lin, L. Lu, W. Cao, T. Li, Hypothesis for potential pathogenesis of SARS-CoV-2 infection——a review of immune changes in patients with viral pneumonia, Emerg. Microb. Infect. (2020) 1–14.
[27] H. Shigeto, H. Tomoya, A. Yukihiro, M. Naoya, I. Taro, S. Masafumi, H. Hideo, T. Osamu, O. Kazunori, S. Takeshi, T. Kazunori, Identification of neutrophil extracellular traps in the blood of patients with systemic inflammatory response syndrome, J. Int. Med. Res. 41 (1) (2013) 162–168.
[28] D. Zhang, R. Guo, L. Lei, H. Liu, Y. Wang, Y. Wang, T. Dai, T. Zhang, Y. Lai, J. Wang, Z. Liu, A. He, M. O'Dwyer, J. Hu, COVID-19 Infection Induces Readily Detectable Morphological and Inflammation-Related Phenotypic Changes in Peripheral Blood Monocytes, the Severity of Which Correlate with Patient Outcome, 03.24.20042655, Medrxiv, 2020, p. 2020.
[29] Y. Zhou, B. Fu, X. Zheng, D. Wang, C. Zhao, Y. Qi, R. Sun, Z. Tian, X. Xu, H. Wei, Pathogenic T-Cells and Inflammatory Monocytes Incite Inflammatory Storms in Severe COVID-19 Patients, National Science Review, 2020.
[30] M.B. Ka, D. Olive, J.-L. Mege, Modulation of monocyte subsets in infectious diseases, World J. Immunol. 4 (3) (2014) 185.
[31] J. Cros, N. Cagnard, K. Woollard, N. Patey, S.-Y. Zhang, B. Senechal, A. Puel, S. K. Biswas, D. Moshous, C. Picard, J.-P. Jais, D. D'Cruz, J.-L. Casanova, C. Trouillet, F. Geissmann, Human CD14dim monocytes patrol and sense nucleic acids and viruses via TLR7 and TLR8 receptors, Immunity 33 (3) (2010) 375–386.
[32] K. Tsukada, T. Kitazawa, A. Fukushima, S. Okugawa, S. Yanagimoto, K. Tatsuno, K. Koike, H. Nagase, K. Hirai, Y. Ota, Macrophage tolerance induced by stimulation with Toll-like receptor 7/8 ligands, Immunol. Lett. 111 (1) (2007) 51–56.
[33] H.W. Ziegler-Heitbrock, A. Wedel, W. Schraut, M. Ströbel, P. Wendelgass, T. Sternsdorf, P.A. Bäuerle, J.G. Haas, G. Riethmüller, Tolerance to lipopolysaccharide involves mobilization of nuclear factor kappa B with predominance of p50 homodimers, J. Biol. Chem. 269 (25) (1994) 17001–17004.
[34] A. Broad, D. Jones, J. Kirby, Toll-like receptor (TLR) response tolerance: a key physiological " damage limitation " effect and an important potential opportunity for therapy, Curr. Med. Chem. 13 (21) (2006) 2487–2502.
[35] S.K. Butcher, C.E. O'Carroll, C.A. Wells, R.J. Carmody, Toll-like receptors drive specific patterns of tolerance and training on restimulation of macrophages, Front. Immunol. 9 (2018) 933.
[36] A. Broad, J.A. Kirby, D.E.J. Jones, Toll-like receptor interactions: tolerance of MyD88-dependent cytokines but enhancement of MyD88-independent interferon-β production, Immunology 120 (1) (2007) 103–111.
[37] H. Weighardt, C.-D. Heidecke, K. Emmanuilidis, S. Maier, H. Bartels, J.-R. Siewert, B. Holzmann, Sepsis after major visceral surgery is associated with sustained and interferon-γ–resistant defects of monocyte cytokine production, Surgery 127 (3) (2000) 309–315.
[38] F. Altare, D. Lammas, P. Revy, E. Jouanguy, R. Döffinger, S. Lamhamedi, P. Drysdale, D. Scheel-Toellner, J. Girdlestone, P. Darbyshire, M. Wadhwa, H. Dockrell, M. Salmon, A. Fischer, A. Durandy, J.-L. Casanova, D. S. Kumararatne, Inherited interleukin 12 deficiency in a child with bacille Calmette-Guérin and Salmonella enteritidis disseminated infection, J. Clin. Invest. 102 (12) (1998) 2035–2040.
[39] S. Haraguchi, N.K. Day, R.P. Nelson, P. Emmanuel, J.E. Duplantier, C. S. Christodoulou, R.A. Good, Interleukin 12 deficiency associated with recurrent infections, Proc. Natl. Acad. Sci. Unit. States Am. 95 (22) (1998) 13125–13129.
[40] T. Hensler, C.D. Heidecke, H. Hecker, K. Heeg, H. Bartels, N. Zantl, H. Wagner, J. R. Siewert, B. Holzmann, Increased susceptibility to postoperative sepsis in patients with impaired monocyte IL-12 production, J. Immunol. 161 (5) (1998) 2655–2659.
[41] P.K. Bhatraju, B.J. Ghassemieh, M. Nichols, R. Kim, K.R. Jerome, A.K. Nalla, A. L. Greninger, S. Pipavath, M.M. Wurfel, L. Evans, P.M. Kritek, T.E. West, A. Luks, A. Gerbino, C.R. Dale, J.D. Goldman, S. O'Mahony, C. Mikacenic, Covid-19 in critically ill patients in the seattle region — case series, N. Engl. J. Med. 382 (2020) 2012–2022.
[42] Y. Liu, X. Du, J. Chen, Y. Jin, L. Peng, H.H.X. Wang, M. Luo, L. Chen, Y. Zhao, Neutrophil-to-lymphocyte ratio as an independent risk factor for mortality in hospitalized patients with COVID-19, J. Infect. 81 (2020) 6–12.
[43] Z. Liu, W. Long, M. Tu, S. Chen, Y. Huang, S. Wang, W. Zhou, D. Chen, L. Zhou, M. Wang, M. Wu, Q. Huang, H. Xu, W. Zeng, L. Guo, Lymphocyte subset (CD4+, CD8+) counts reflect the severity of infection and predict the clinical outcomes in patients with COVID-19, J. Infect. 81 (2020) 318–356.
[44] J. Phua, L. Weng, L. Ling, M. Egi, C.-M. Lim, J.V. Divatia, B.R. Shrestha, Y. M. Arabi, J. Ng, C.D. Gomersall, M. Nishimura, Y. Koh, B. Du, A.C.C.C.T. Group, Intensive care management of coronavirus disease 2019 (COVID-19): challenges and recommendations, Lancet Respir. Med. 8 (2020) 506–517.
[45] J.T. Poston, B.K. Patel, A.M. Davis, Management of critically ill adults with COVID-19, JAMA 323 (16) (2020).
[46] C. Qin, L. Zhou, Z. Hu, S. Zhang, S. Yang, Y. Tao, C. Xie, K. Ma, K. Shang, W. Wang, D.-S. Tian, Dysregulation of Immune Response in Patients with COVID-19 in Wuhan, China, Clin Infect Dis Official Publ Infect Dis Soc Am, 2020.
[47] Q. Ruan, K. Yang, W. Wang, L. Jiang, J. Song, Clinical predictors of mortality due to COVID-19 based on an analysis of data of 150 patients from Wuhan, China, Intensive Care Med. (2020) 1–3.
[48] G. Srikrishna, H.H. Freeze, Endogenous damage-associated molecular pattern molecules at the crossroads of inflammation and cancer, Neoplasia 11 (7) (2009) 615–628.
[49] S. Ivanov, A.-M.M. Dragoi, X. Wang, C. Dallacosta, J. Louten, G. Musco, G. Sitia, G.S. Yap, Y. Wan, C.A. Biron, M.E. Bianchi, H. Wang, W.-M.M. Chu, A novel role for HMGB1 in TLR9-mediated inflammatory responses to CpG-DNA, Blood 110 (6) (2007) 1970–1981.
[50] M. Haghbin, M. Rostami-Nejad, F. Forouzesh, A. Sadeghi, K. Rostami, E. Aghamohammadi, H. Asadzadeh-Aghdaei, A. Masotti, M.R. Zali, The role of CXCR3 and its ligands CXCL10 and CXCL11 in the pathogenesis of celiac disease, Medicine 98 (25) (2019) e15949-e15949.
[51] H. Shaath, R. Vishnubalaji, E. Elkord, N.M. Alajez, Single-cell transcriptome analysis highlights a role for neutrophils and inflammatory macrophages in the pathogenesis of severe COVID-19, Cells 9 (11) (2020), 2374-2374.
[52] K.A. Gauss, L.K. Nelson-Overton, D.W. Siemsen, Y. Gao, F.R. DeLeo, M.T. Quinn, Role of NF-κB in transcriptional regulation of the phagocyte NADPH oxidase by tumor necrosis factor-α, J. Leukoc. Biol. 82 (3) (2007) 729–741.
[53] S. Khanmohammadi, N. Rezaei, Role of Toll-like receptors in the pathogenesis of COVID-19, J. Med. Virol. 93 (5) (2021) 2735–2739.
[54] M. Mahler, P.-L. Meroni, M. Infantino, K.A. Buhler, M.J. Fritzler, Circulating calprotectin as a biomarker of COVID-19 severity, Expet Rev. Clin. Immunol. 17 (5) (2021) 431–443.
[55] R. Förster, A.C. Davalos-Misslitz, A. Rot, CCR7 and its ligands: balancing immunity and tolerance, Nat. Rev. Immunol. 8 (5) (2008) 362–371.
[56] H. Higuchi, T. Shoji, S. Iijima, K.-i. Nishijima, Constitutively expressed Siglec-9 inhibits LPS-induced CCR7, but enhances IL-4-induced CD200R expression in human macrophages, Biosci. Biotechnol. Biochem. 80 (6) (2016) 1141–1148.
[57] S. Li, T. Miao, M. Sebastian, P. Bhullar, E. Ghaffari, M. Liu, A.L.J. Symonds, P. Wang, The transcription factors Egr 2 and Egr3 are essential for the control of inflammation and antigen-induced proliferation of B and T cells, Immunity 37 (4) (2012) 685–696.
[58] N. Chevrier, P. Mertins, M.N. Artyomov, A.K. Shalek, M. Iannacone, M.F. Ciaccio, I. Gat-Viks, E. Tonti, M.M. DeGrace, K.R. Clauser, M. Garber, T.M. Eisenhaure, N. Yosef, J. Robinson, A. Sutton, M.S. Andersen, D.E. Root, U. von Andrian, R. B. Jones, H. Park, S.A. Carr, A. Regev, I. Amit, N. Hacohen, Systematic discovery of TLR signaling components delineates viral-sensing circuits, Cell 147 (4) (2011) 853–867.
[59] M. Saichi, M.Z. Ladjemi, S. Korniotis, C. Rousseau, Z. Ait Hamou, L. Massenet-Regad, E. Amblard, F. Noel, Y. Marie, D. Bouteiller, J. Medvedovic, F. Pène,

V. Soumelis, Single-cell RNA sequencing of blood antigen-presenting cells in severe COVID-19 reveals multi-process defects in antiviral immunity, Nat. Cell Biol. 23 (5) (2021) 538–551.
[60] C. Zhang, N. Bai, A. Chang, Z. Zhang, J. Yin, W. Shen, Y. Tian, R. Xiang, C. Liu, ATF4 is directly recruited by TLR4 signaling and positively regulates TLR4-trigged cytokine production in human monocytes, Cell. Mol. Immunol. 10 (1) (2013) 84–94.
[61] D.M. Cohen, K.-J. Won, N. Nguyen, M.A. Lazar, C.S. Chen, D.J. Steger, ATF4 licenses C/EBPβ activity in human mesenchymal stem cells primed for adipogenesis, Elife 4 (2015).
[62] T. Kawai, S. Akira, TLR signaling, Semin. Immunol. 19 (1) (2007) 24–32.
[63] T. Kawai, S. Akira, Signaling to NF-kappaB by toll-like receptors, Trends Mol. Med. 13 (11) (2007) 460–469.
[64] T. Kaisho, S. Akira, Toll-like receptor function and signaling, J. Allergy Clin. Immunol. 117 (5) (2006) 979.
[65] T. Kawai, S. Akira, Signaling to NF-kappaB by toll-like receptors, Trends Mol. Med. 13 (11) (2007) 460–469.
[66] A. Adelaja, A. Hoffmann, Signaling crosstalk mechanisms that may fine-tune pathogen-responsive NFκB, Front. Immunol. 10 (2019).
[67] N. Borregaard, O.E. Sørensen, -.M.K. Theilgaard, Neutrophil granules: a library of innate immunity proteins, Trends Immunol. 28 (8) (2007) 340–345.
[68] L.R. Prince, M.K. Whyte, I. Sabroe, L.C. Parker, The role of TLRs in neutrophil activation, Curr. Opin. Pharmacol. 11 (4) (2011) 397–403.
[69] F. Hayashi, T.K. Means, A.D. Luster, Toll-like Receptors Stimulate Human Neutrophil Function, Blood, 2003.
[70] F. Krisztina, F. Szabina, M. Attila, Neutrophil cell surface receptors and their intracellular signal transduction pathways, Int. Immunopharm. 17 (3) (2013).
[71] T.H. Flo, K.D. Smith, S. Sato, D.J. Rodriguez, M.A. Holmes, R.K. Strong, S. Akira, A. Aderem, Lipocalin 2 mediates an innate immune response to bacterial infection by sequestrating iron, Nature 432 (7019) (2004) 917–921.
[72] S. Geetha, S100A8 and S100A9: new insights into their roles in malignancy, J. Innate Immun. 4 (1) (2011) 31–40.
[73] S. Mukhopadhyay, A. Varin, Y. Chen, B. Liu, K. Tryggvason, S. Gordon, SR-A/MARCO–mediated ligand delivery enhances intracellular TLR and NLR function, but ligand scavenging from cell surface limits TLR4 response to pathogens, Blood 117 (4) (2011) 1319–1328.
[74] K. Komai, T. Shichita, M. Ito, M. Kanamori, S. Chikuma, A. Yoshimura, Role of scavenger receptors as damage-associated molecular pattern receptors in Toll-like receptor activation, Int. Immunol. 29 (2) (2017) 59–70.
[75] Y.-l. Jiao, M.-P. Wu, Apolipoprotein A-I diminishes acute lung injury and sepsis in mice induced by lipoteichoic acid, Cytokine 43 (1) (2008) 83–87.
[76] K. Georgila, D. Vyrla, E. Drakos, Apolipoprotein A-I (ApoA-I), immunity, inflammation and cancer, Cancers 11 (8) (2019) 1097.
[77] M.M. Wurfel, S.T. Kunitake, H. Lichenstein, J.P. Kane, S.D. Wright, Lipopolysaccharide (LPS)-binding protein is carried on lipoproteins and acts as a cofactor in the neutralization of LPS, J. Exp. Med. 180 (3) (1994) 1025–1035.
[78] M. Monguió-Tortajada, M. Franquesa, M.-R. Sarrias, F.E. Borràs, Low doses of LPS exacerbate the inflammatory response and trigger death on TLR3-primed human monocytes, Cell Death Dis. 9 (5) (2018) 499.
[79] C. Dong, R.J. Davis, R.A. Flavell, Map kinases in the immune response, Annu. Rev. Immunol. 20 (1) (2002) 55–72.
[80] H.T. Lu, D.D. Yang, M. Wysk, E. Gatti, I. Mellman, R.J. Davis, R.A. Flavell, Defective IL-12 production in mitogen-activated protein (MAP) kinase kinase 3 (Mkk3)-deficient mice, EMBO J. 18 (7) (1999) 1845–1857.
[81] A. Nansen, A.R. Thomsen, Viral infection causes rapid sensitization to lipopolysaccharide: central role of IFN-αβ, J. Immunol. 166 (2) (2001) 982–988.
[82] Z. Xu, Y. Tang, Q. Huang, S. Fu, X. Li, B. Lin, A. Xu, J. Chen, Systematic review and subgroup analysis of the incidence of acute kidney injury (AKI) in patients with COVID-19, BMC Nephrol. 22 (1) (2021) 52.
[83] C.-E. Luyt, T. Sahnoun, M. Gautier, P. Vidal, S. Burrel, M.P.d. Chambrun, J. Chommeloux, C. Desnos, J. Arzoine, A. Nieszkowska, N. Bréchot, M. Schmidt, G. Hekimian, D. Boutolleau, J. Robert, A. Combes, J. Chastre, Ventilator-associated pneumonia in patients with SARS-CoV-2-associated acute respiratory distress syndrome requiring ECMO: a retrospective cohort study, Ann. Intensive Care 10 (1) (2020) 158.
[84] K.A. Davis, Ventilator-associated pneumonia: a review, J. Intensive Care Med. 21 (4) (2006) 211–226.
[85] K.F.v.d. Sluijs, T.v.d. Poll, R. Lutter, N.P. Juffermans, M.J. Schultz, Bench-to-bedside review: bacterial pneumonia with influenza - pathogenesis and clinical implications, Crit. Care 14 (2) (2010) 219.
[86] A. Nansen, J.P. Christensen, O. Marker, A.R. Thomsen, Sensitization to lipopolysaccharide in mice with asymptomatic viral infection: role of T cell-dependent production of interferon-γ, J. Infect. Dis. 176 (1) (1997) 151–157.
[87] C. Tang, S. Ye, H. Liu, Electrospinning of poly(styrene-co-maleic anhydride) (SMA) and water-swelling behavior of crosslinked/hydrolyzed SMA hydrogel nanofibers, Polymer 48 (15) (2007) 4482–4491.
[88] O. Stoilova, M. Ignatova, N. Manolova, T. Godjevargova, D.G. Mita, I. Rashkov, Functionalized electrospun mats from styrene–maleic anhydride copolymers for immobilization of acetylcholinesterase, Eur. Polym. J. 46 (10) (2010) 1966–1974.
[89] M. Ignatova, O. Stoilova, N. Manolova, N. Markova, I. Rashkov, Electrospun mats from styrene/maleic anhydride copolymers: modification with amines and assessment of antimicrobial activity, Macromol. Biosci. 10 (8) (2010) 944–954.
[90] T. Stuart, A. Butler, P. Hoffman, C. Hafemeister, E. Papalexi, W.M. Mauck, Y. Hao, M. Stoeckius, P. Smibert, R. Satija, Comprehensive integration of single-cell data, Cell 177 (7) (2019) 1888–1902, e21.
[91] I. Korsunsky, N. Millard, J. Fan, K. Slowikowski, F. Zhang, K. Wei, Y. Baglaenko, M. Brenner, P.-r. Loh, S. Raychaudhuri, Fast, sensitive and accurate integration of single-cell data with Harmony, Nat. Methods 16 (12) (2019) 1289–1296.
[92] D. Aran, A.P. Looney, L. Liu, E. Wu, V. Fong, A. Hsu, S. Chak, R.P. Naikawadi, P. J. Wolters, A.R. Abate, A.J. Butte, M. Bhattacharya, Reference-based analysis of lung single-cell sequencing reveals a transitional profibrotic macrophage, Nat. Immunol. 20 (2) (2019) 163–172.
[93] J. Alquicira-Hernandez, J.E. Powell, Nebulosa recovers single-cell gene expression signals by kernel density estimation, Bioinformatics 37 (2021) 2485–2487.
[94] M.D. Robinson, D.J. McCarthy, G.K. Smyth, edgeR: a Bioconductor package for differential expression analysis of digital gene expression data, Bioinformatics 26 (1) (2010) 139–140.
[95] D.J. McCarthy, Y. Chen, G.K. Smyth, Differential expression analysis of multifactor RNA-Seq experiments with respect to biological variation, Nucleic Acids Res. 40 (10) (2012) 4288–4297.
[96] J.R. Conway, A. Lex, N. Gehlenborg, UpSetR: an R package for the visualization of intersecting sets and their properties, Bioinformatics 33 (18) (2017) 2938–2940.
[97] U. Raudvere, L. Kolberg, I. Kuzmin, T. Arak, P. Adler, H. Peterson, J. Vilo, g: Profiler: a web server for functional enrichment analysis and conversions of gene lists (2019 update), Nucleic Acids Res. 47 (W1) (2019) W191–W198.
[98] E.J. Fertig, J. Ding, A.V. Favorov, G. Parmigiani, M.F. Ochs, CoGAPS: an R/C++ package to identify patterns and biological process activity in transcriptomic data, Bioinformatics 26 (21) (2010) 2792–2793.
[99] S. Aibar, C.B. González-Blas, T. Moerman, V.A. Huynh-Thu, H. Imrichova, G. Hulselmans, F. Rambow, J.-C. Marine, P. Geurts, J. Aerts, J. van den Oord, Z. K. Atak, J. Wouters, S. Aerts, SCENIC: single-cell regulatory network inference and clustering, Nat. Methods 14 (11) (2017) 1083–1086.
[100] B. Van de Sande, C. Flerin, K. Davie, M. De Waegeneer, G. Hulselmans, S. Aibar, R. Seurinck, W. Saelens, R. Cannoodt, Q. Rouchon, T. Verbeiren, D. De Maeyer, J. Reumers, Y. Saeys, S. Aerts, A scalable SCENIC workflow for single-cell gene regulatory network analysis, Nat. Protoc. 15 (7) (2020) 2247–2276.
[101] M. Kanehisa, KEGG: kyoto encyclopedia of genes and genomes, Nucleic Acids Res. 28 (1) (2000) 27–30.
[102] D. Szklarczyk, A.L. Gable, D. Lyon, A. Junge, S. Wyder, J. Huerta-Cepas, M. Simonovic, N.T. Doncheva, J.H. Morris, P. Bork, L.J. Jensen, C.v. Mering, STRING v11: protein–protein association networks with increased coverage, supporting functional discovery in genome-wide experimental datasets, Nucleic Acids Res. 47 (D1) (2019) D607–D613.
[103] D. Merico, R. Isserlin, O. Stueker, A. Emili, G.D. Bader, Enrichment map: a network-based method for gene-set enrichment visualization and interpretation, PLoS One 5 (11) (2010) e13984-e13984.
[104] P. Shannon, Cytoscape: a software environment for integrated models of biomolecular interaction networks, Genome Res. 13 (11) (2003) 2498–2504.